The Turbulent Structure and Diurnal Growth of the Saharan Atmospheric Boundary Layer

L. GARCIA-CARRERAS

*Department of Meteorology, and the Bert Bolin Centre for Climate Research,
Stockholm University, Stockholm, Sweden*

D. J. PARKER, J. H. MARSHAM, P. D. ROSENBERG, AND I. M. BROOKS

Institute for Climate and Atmospheric Sciences, University of Leeds, Leeds, United Kingdom

A. P. LOCK AND F. MARENCO

Met Office, Exeter, United Kingdom

J. B. MCQUAID

Institute for Climate and Atmospheric Sciences, University of Leeds, Leeds, United Kingdom

M. HOBBY

National Centre for Atmospheric Science, University of Leeds, Leeds, United Kingdom

ABSTRACT

The turbulent structure and growth of the remote Saharan atmospheric boundary layer (ABL) is described with in situ radiosonde and aircraft measurements and a large-eddy simulation model. A month of radiosonde data from June 2011 provides a mean profile of the midday Saharan ABL, which is characterized by a well-mixed convective boundary layer, capped by a small temperature inversion (<1 K) and a deep, near-neutral residual layer. The boundary layer depth varies by up to 100% over horizontal distances of a few kilometers due to turbulent processes alone. The distinctive vertical structure also leads to unique boundary layer processes, such as detrainment of the warmest plumes across the weak temperature inversion, which slows down the warming and growth of the convective boundary layer. As the boundary layer grows, overshooting plumes can also entrain free-tropospheric air into the residual layer, forming a second entrainment zone that acts to maintain the inversion above the convective boundary layer, thus slowing down boundary layer growth further. A single-column model is unable to accurately reproduce the evolution of the Saharan boundary layer, highlighting the difficulty of representing such processes in large-scale models. These boundary layer processes are special to the Sahara, and possibly hot, dry, desert environments in general, and have implications for the large-scale structure of the Saharan heat low. The growth of the boundary layer influences the vertical redistribution of moisture and dust, and the spatial coverage and duration of clouds, with large-scale dynamical and radiative implications.

1. Introduction

The Saharan atmosphere is a key component of the climate system. Intense solar heating during the boreal summer leads to the formation of a near-surface low pressure system known as the Saharan heat low, which is a major element of the West African monsoon, strengthening the moist, southwesterly monsoon flow from the ocean, as well as the dry Harmattan flow in the north and east (Parker et al. 2005; Lavaysse et al. 2009). The Sahara is also the world's largest source of mineral dust (Prospero

Corresponding author address: L. Garcia-Carreras, Department of Meteorology, Stockholm University, Stockholm 10691, Sweden. E-mail: luis.garciacarreras@misu.su.se

et al. 2002; Washington et al. 2003), which has significant implications for both regional and global climate, via both its direct interaction with radiation (Haywood and Boucher 2000) and its impacts on cloud microphysical processes (Kaufman et al. 2005). The long-range transport and deposition of mineral dust has also been shown to interact with biogeochemical cycles in remote regions (e.g., Jickells et al. 2005).

The Saharan atmospheric boundary layer (ABL) controls the vertical redistribution and transport of dust, heat, moisture, and momentum within the Saharan heat low region (Cuesta et al. 2009). As a result of the extreme near-surface temperatures, the Saharan ABL commonly reaches 5–6 km, making it probably the deepest on earth (Gamo 1996). In the morning and early afternoon a small temperature inversion, typically ≤ 1 K over a depth of around 100 m, separates the Saharan convective boundary layer (CBL) from a deep near-neutral Saharan residual layer (RL), with a lapse rate of approximately 1 K km^{-1}, caused by the previous day's fully developed CBL (Messager et al. 2010). The CBL often reaches its full extent only in the late afternoon (Marsham et al. 2013b), and radiosonde observations show that the RL can sometimes persist over large areas throughout the day (Cuesta et al. 2008; Messager et al. 2010; Marsham et al. 2013b). This persistence of the RL can be explained by subsidence, caused either by mesoscale circulations induced by albedo variations (Marsham et al. 2008) or larger-scale features like the Hoggar Mountains in the east (Birch et al. 2012), which suppresses the CBL growth. Air from the Atlantic advected into the Sahara can lead to a persistent shallow CBL (Marsham et al. 2013b) and Saharan air advected farther south into the Sahel also displays similar characteristics to the Saharan RL (Canut et al. 2010). The large depth of the Saharan ABL allows boundary layer clouds to form via adiabatic cooling, despite the dry conditions, and small errors in humidity in models can have substantial impacts on modeled cloud cover, and thus radiation (Flamant et al. 2007; Messager et al. 2010; Marsham et al. 2013b). It is hypothesized that the small temperature inversion separating the CBL from the RL means that small perturbations in CBL temperature can have a large impact on vertical mixing and that they also induce thermally driven circulations that affect the CBL at the mesoscale (Marsham et al. 2008). Modeling studies provide some evidence to support these ideas (Huang et al. 2010; Birch et al. 2012). There is some evidence that the diurnal cycle in BL drag on winds at these levels results in an "upper Saharan BL jet" during the morning, analogous to the well-known nocturnal low-level jet (Marsham et al. 2013b), which affects synoptic-scale transport. The growth of the CBL leads to the breakdown of the nocturnal low-level jet by

entraining and mixing down the high-momentum air, thus producing a rapid increase in near-surface wind speeds and dust emission in the morning (Fiedler et al. 2013). There is also evidence from ground-based data that, similar to the low-level jet breakdown, the downward mixing of the upper Saharan BL winds also causes an afternoon maximum in dust emission (Todd et al. 2013).

Despite the importance of the Sahara for the climate system, routine observations are sparse and the few data that exist are mostly from the periphery of the desert, thus missing the center of the heat low. This leads to large disagreements between analyses (Marsham et al. 2011) and significant biases in operational (Agustí-Panareda et al. 2010; Garcia-Carreras et al. 2013) and climate models (Roehrig et al. 2013) and fundamentally limits our process-based understanding of the Saharan heat low. The subtle vertical structure of the Saharan boundary layer, in particular the residual layer, provides additional challenges for boundary layer parameterizations (Couvreux et al. 2014). The Fennec project is a large-scale, international observational and modeling program that aimed to produce the most comprehensive dataset of the central Saharan atmosphere to date (Washington et al. 2012). The observational program included two ground-based supersites, one of which was located at Bordj Badji Mokhtar (BBM), southern Algeria, close to the climatological location of the Saharan heat low (Marsham et al. 2013b), with the other supersite farther west (Todd et al. 2013). Two aircraft campaigns also took place during June 2011 and 2012 from a base in Fuerteventura (Ryder et al. 2013); these included the first-ever flights to sample the vertical structure of the Saharan ABL using an extensive suite of onboard instrumentation.

In this study we aim to describe the characteristics of a typical Saharan ABL, particularly the turbulent and vertical mixing between its various layers and its diurnal evolution. We use a combination of large-eddy modeling and the unique radiosonde and aircraft observations taken in the central Sahara during Fennec, which are described in section 2. A climatology of the radiosonde data is used to describe the mean structure of the Saharan ABL in section 3a, providing the context for the subsequent detailed analysis. Limitations in the aircraft data, described in section 2a, make their interpretation difficult. For this reason, the large-eddy simulation results are used in section 3b to investigate the variability of the Saharan ABL, and the key processes governing its diurnal evolution, while in section 3c aircraft data are used to provide supporting evidence for the specific processes described in the model. A single-column model version of the Met Office Unified Model is used to evaluate the ability of large-scale models to represent the Saharan ABL in section 3d, before summarizing the results in section 4.
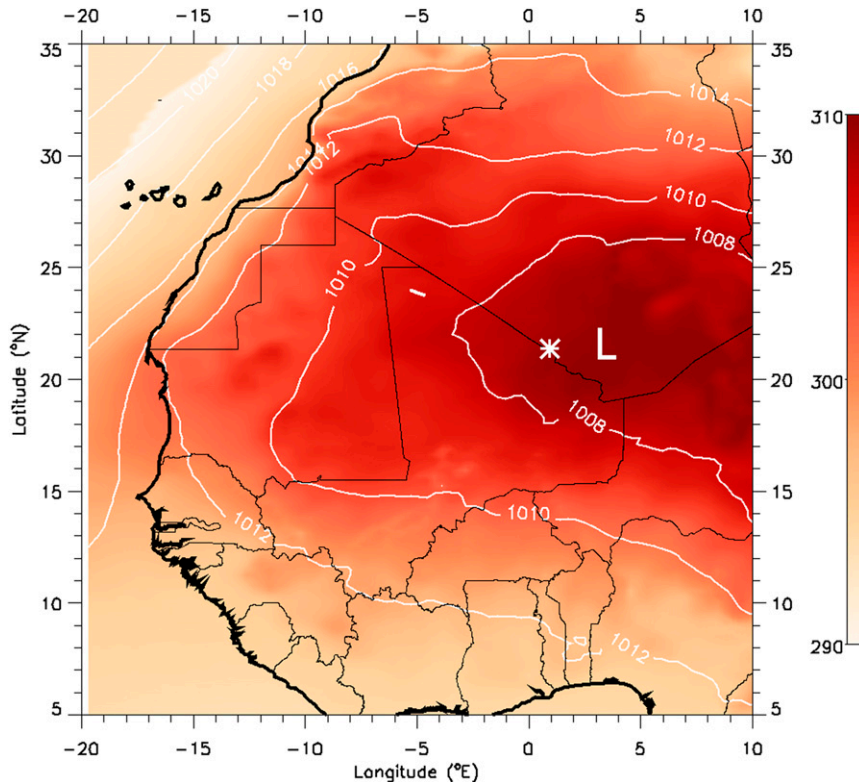
FIG. 1. Met Office Unified Model analysis 925-mb potential temperature (colors) and mean sea level pressure (white lines) averaged over June 2011. The letter L indicates the approximate mean location of the Saharan heat low. The star shows the location of the radiosonde station at Bordj Badji Mokhtar, and the white straight line is the aircraft path.

2. Method

a. Observations

We use radiosondes and eddy covariance estimates of surface fluxes from Fennec supersite-1 at BBM in the central Sahara (star in Fig. 1, with solar noon at 1157 UTC 15 June) to initialize, force, and compare with the Met Office Large Eddy Model (LEM) simulation. Vaisala RS92 radiosondes were launched at 3–6-h intervals during 8–30 June 2011, providing the first continuous in situ measurements of the vertical structure of the remote Saharan atmosphere close to the climatological location of the Saharan heat low (indicated by the letter L in Fig. 1). Conditions were generally moister and drier after 18 June, but there was no clear seasonal variation in the Saharan ABL structure during this period [Marsham et al. (2013b) provides a comprehensive review of the supersite and the conditions throughout this month]. The measurements were used to construct mean profiles of the Saharan ABL at BBM to show to what extent the modeling results represent recurrent features in the observations. A 0900 UTC profile from 20 June 2011 was used to initialize the LEM (section 2b). This day was

chosen because the midday temperature profile was representative of a typical Saharan ABL and the CBL grew to a height of 500 mb (1 mb = 1 hPa) by the end of the day, with little influence from synoptic processes.

Aircraft measurements from a flight that took place between 1300 and 1515 UTC 12 June 2012 over northern Mali are used to compare with the modeling results [flight B705, white line in Fig. 1, see Ryder et al. (2013) for more details on the aircraft campaign]. Data used include temperature and three-dimensional wind observations at 32 Hz. A Leosphere ALS450 elastic backscatter lidar with daytime capability was used on board the aircraft. The lidar was pointing at nadir and had an operational wavelength of 355 nm and overlap range of 300 m. The data used have a vertical resolution of 225 m and an integration time of 20 s; at typical aircraft speeds, the latter translates into a ~3-km footprint. The flight took the form of straight, stacked legs of ~60 km in length—long enough for fluxes to be calculated with the eddy covariance method. By their very nature, the measurements are limited, both spatially and temporally, and complicated by the heterogeneous conditions along the flight track as well as the simultaneous time

and height evolution of the boundary layer while performing the stacked legs. However, these data provide unprecedented detail of the turbulent characteristics of the Saharan ABL and can be used to validate the processes identified with the model.

b. Large-eddy simulation model

We use version 2.4 of the Met Office Large Eddy Model (LEM) (Gray et al. 2001), a state-of-the-art model for large-eddy simulation and cloud-resolving modeling, to identify and describe the primary processes that control the vertical structure and turbulent mixing processes in the Saharan ABL. The LEM is a nonhydrostatic model with a Boussinesq equation set, using a k-closure and a 3D turbulence scheme. A $30 \times 30 \times 8\,km^3$ domain with periodic lateral boundary conditions was used with a horizontal grid spacing of 60 m and a variable vertical grid spacing of 11–60 m, with highest resolution within the boundary layer and at the residual-layer top, where shear-induced mixing could be important. The resolution is slightly coarser than that typically used to study boundary layer turbulence; the large depth of the Saharan ABL means that a large domain is needed, limiting the resolution at which the model can be run. The turbulent length scales will, however, scale accordingly, so a coarser resolution is adequate. A layer damping the prognostic variables to their horizontal means was applied above 7500 m to reduce the reflection of gravity waves from the upper boundary. The model was run from 0900 to 1800 UTC, initialized with a radiosounding launched at 0900 UTC 20 June 2011 from the Fennec supersite-1 at BBM. The time-varying surface sensible heat fluxes were prescribed with a diurnal cycle of eddy-covariance measurements taken at BBM for the same day, smoothed with a 1-h running mean. A passive tracer was initialized at the start of the run as a spatially homogeneous layer at the lowest model level in order to better visualize the mixing and transport in the CBL, as well as acting as a proxy for boundary layer aerosol such as dust. The model is run with both the radiation and microphysics schemes turned off and without any large-scale forcing, such as large-scale subsidence in relation to the descending motion of the Hadley cell. The objective of the simulation is not to reproduce this particular day at BBM, but to describe the general characteristics and daytime evolution of a typical Saharan ABL.

c. Single-column model simulation

To evaluate the ability of large-scale models to represent the evolution of the Saharan ABL, the Met Office Unified Model (Walters et al. 2014) was run as a single-column model (SCM) with the same initial conditions and surface fluxes as the LEM (see section 2b).

Radiation was switched off (as in the LEM) so that only the boundary layer parameterization (Brown et al. 2008) was actually used. Although the cloud and cumulus convection parameterizations were switched on, no clouds were formed during the simulation, so these parameterizations were never triggered. The boundary layer parameterization is a first-order turbulence closure where, for unstable boundary layers, the diffusion coefficients are specified functions of height within the boundary layer, related to the strength of the turbulence. There are additional parameterized nonlocal flux profiles of heat and momentum that have the effect of generating more vertically uniform potential temperature and wind profiles in convective boundary layers. The existence and depth of unstable layers is diagnosed by lifting a moist adiabatic parcel to its level of neutral buoyancy. Mixing across the top of the boundary layer is through an explicit entrainment parameterization dependent in the simulations here on the surface buoyancy flux, friction velocity, and inversion strength (Lock et al. 2000). For stable boundary layers and in the free troposphere, a local Richardson number–dependent scheme is used (Brown et al. 2008).

The SCM was run with two different time steps: 15 min, representing a typical operational value, and 1 min. The vertical grid from the operational global configurations is used, which has 62 levels below 40 km with the spacing increasing quadratically with height above the surface, to give a spacing of around 300 m at 3 km. Two finer grids are also tested, both with a 1-min time step. The finest grid has 140 levels with a spacing of 90 m at 3 km and the intermediate grid has 70 levels with a spacing of 200 m at 3 km.

3. Results

a. Mean Saharan ABL vertical profile observed at Fennec supersite-1

Figure 2a shows the mean atmospheric profile over BBM for 23 radiosondes launched at 1200 UTC (1145 local time) during June 2011. Each profile was normalized to its own CBL and RL depths, then rescaled to the mean of all CBL and RL depths (820 ± 80 and 550 ± 50 mb, respectively) before averaging all of the profiles to construct a mean profile of the Saharan ABL (Fig. 2). The CBL and RL heights were determined subjectively, by identifying temperature inversions, coincident with consistent changes in humidity and winds. Only the midday profile is shown as radiosondes on all days were only available at 6-hourly intervals, and profiles at dawn and dusk are complicated by the transition from daytime to nighttime conditions. The modeling results in section 3b
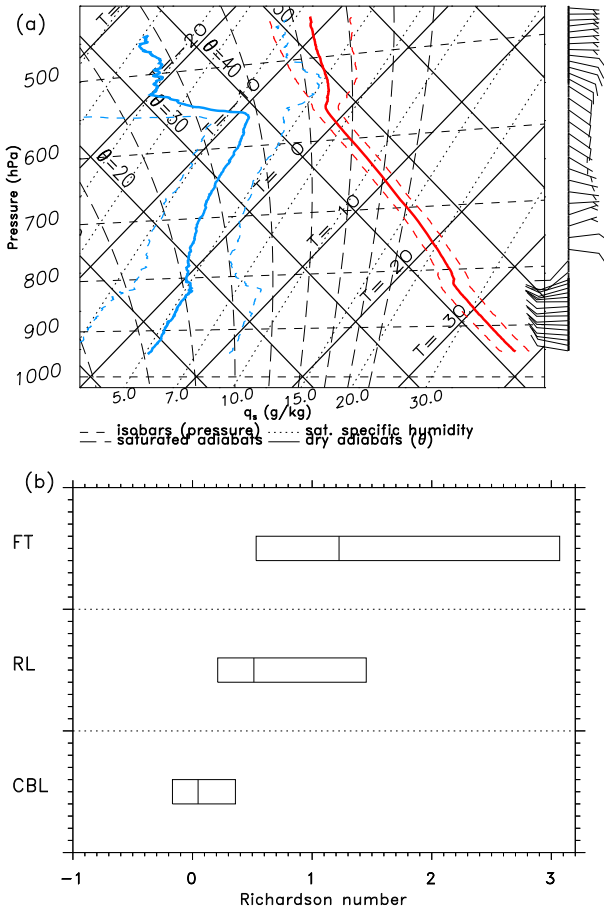
FIG. 2. All 1200 UTC radiosondes launched during 8–30 Jun 2011 (23 in total) normalized to each single CBL and RL top before averaging: (a) mean tephigram with wind barbs and (b) boxplot showing the 25th, 50th, and 75th percentiles of the gradient Richardson number in each layer.

also show that the general structure of the profile in Fig. 2 persists throughout most of the afternoon.

There are a number of features of the Saharan ABL that set it apart from a typical boundary layer. At 1200 UTC, before the CBL has time to fully develop, the Saharan ABL is made up of an actively growing CBL, driven by high sensible heating at the surface, capped by a very weak inversion (often ≤1 K over 10–20 mb in height), with a deep, near-neutral RL above it, produced by the previous day's CBL. The rapid change in wind direction between the CBL and RL is consistent with these two layers being decoupled, despite the small temperature inversion separating them, with the RL winds aligning more closely with the free-tropospheric winds above. The weak stability observed in the residual layer can be explained by the presence of shear at the RL top, which will transport warm, free-tropospheric air downward, although radiative effects from dust and water

vapor have also been suggested as contributing factors (Cuesta et al. 2009). The mean lapse rate in the RL was 1 K km^{-1}, although this value was frequently lower, as a small number of cases with a more stable profile above the inversion dominate the average. This structure is consistent with past observations of the Saharan boundary layer (Messager et al. 2010). The presence of such a weak capping inversion is expected to make the evolution of the Saharan ABL hard to represent in global models, as the ABL will likely be sensitive to the surface fluxes and vertical resolution of the model. The RL typically reaches heights of 550 mb. Despite the strong sensible heating at the surface, the CBL typically erodes the temperature inversion completely only by late afternoon, and in some cases does not reach the top of the RL at all (Cuesta et al. 2008; Messager et al. 2010; Marsham et al. 2013b).

The presence of a weak inversion and a near-neutral residual layer both reduce the return force on overshooting parcels from the CBL relative to the usual case of a CBL capped by a stratified troposphere. Assuming no entrainment, the distance traveled by an overshooting plume h can be estimated theoretically by considering (very simply) the transfer of kinetic to potential energy:

$$h = \frac{w^2}{2g(T/T_0 - 1)}, \qquad (1)$$

where w is the vertical velocity of the plume at the temperature inversion, T and T_0 are the temperatures of the parcel and environment respectively, and g is gravitational acceleration. For a 10 m s^{-1} updraft with a 0.5-K temperature deficit, which represents the most extreme case in the aircraft observations, the overshooting distance is 3300 m. This is likely to represent an upper bound, as many updrafts are weaker, the inversion can be stronger, and the RL is often slightly stable. Entrainment into the plume will reduce its temperature difference from the environment but also reduce its momentum. This simple calculation, however, does show that it is feasible for parcels to travel far into the residual layer, as hypothesized in Huang et al. (2010), without the need for particularly hot plumes in the CBL.

The large distance traveled by overshooting parcels within a near-neutral layer raises the possibility that turbulence in the CBL may induce vertically extensive mixing in the RL, or even lead to detrainment from the CBL top into the RL akin to cumulus detrainment, albeit without the presence of diabatic warming. This would be a unique feature of the Saharan ABL (or perhaps deep, dry desert boundary layers in general) and has implications for the diurnal evolution of the CBL, as well as the
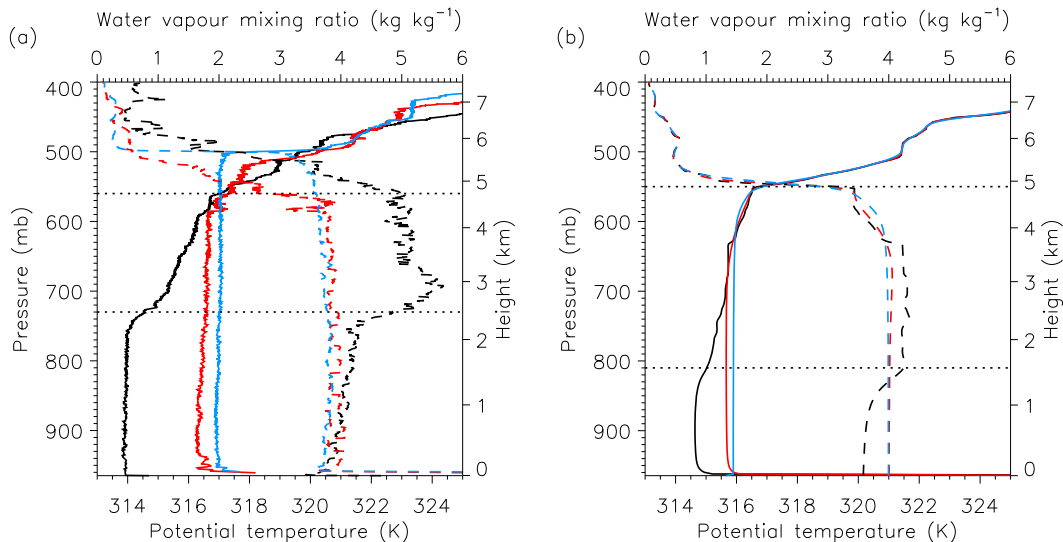
FIG. 3. Vertical profiles of potential temperature (solid lines) and water vapor mixing ratio (dashed lines) at 1200 (black), 1500 (red), and 1800 UTC (blue) in (a) BBM radiosondes launched on 20 Jun 2011 and (b) the LEM simulation. The horizontal dotted lines show the CBL and RL top heights at 1200 UTC.

vertical, and subsequent horizontal long-range, transport of recently uplifted dust.

The gradient Richardson number, Ri, is a dimensionless quantity representing the ratio between shear and buoyant forcing and is a measure of the instability in the atmosphere:

$$Ri = \frac{\dfrac{g}{T_v}\dfrac{\partial \theta_v}{\partial z}}{\left(\dfrac{\partial U}{\partial z}\right)^2 + \left(\dfrac{\partial V}{\partial z}\right)^2}, \qquad (2)$$

where θ_v is virtual potential temperature, T_v is virtual absolute temperature, z is height, and (U, V) are the zonal and meridional wind components. Where $Ri < 0$ the atmosphere is convectively unstable, and where $0 < Ri < 0.25$ the atmosphere is turbulent due to mechanical generation by shear. Where $Ri > 1$ the atmosphere is not turbulent. The values in between $(0.25 < Ri < 1)$ represent a regime where the atmosphere maintains its current state, be it laminar or turbulent. This is due to the fact that laminar flow becomes turbulent when $Ri < 0.25$, but turbulent flow becomes laminar when $Ri > 1$, producing a hysteresis effect (Galperin et al. 2007; Stull 1988). Figure 2b shows boxplots of the gradient Richardson number in each layer for all the 1200 UTC BBM radiosondes. In the CBL, the atmosphere is turbulent $(Ri < 0.25)$ on most days. The free troposphere, on the other hand, is almost never unstable, and has $Ri > 1$ on most days. Conditions in the RL are more complex. Shear-induced turbulence is significant, particularly close to the RL top (30% of days with $0 < Ri < 0.25$), while the

largest proportion of days have $0.25 < Ri < 1$, where turbulent mixing is not generated, but can be maintained. Radiosonde wind profiles show that wind shear is a recurrent feature both at the CBL and RL tops, and may therefore be a significant contributor to turbulence and mixing in, and between, both layers (not shown).

b. Large-eddy modeling of the Saharan ABL

1) VALIDATION OF THE SAHARAN ABL STRUCTURE IN THE LEM SIMULATION

The evolution of the Saharan ABL in the LEM can be compared to radiosonde data for the same day used for the initialization. The idealized modeling approach means that an exact match is not expected, particularly because in the LEM the extent of CBL development is controlled solely by the initial profile and surface fluxes, with no impacts from external factors or some missing processes (discussed below). It is important, however, to determine whether the LEM is representative of reality, despite these deficits.

Overall, the model can reproduce the general Saharan ABL structure and its diurnal evolution (Fig. 3). At 0900 UTC, when the model is initialized, the nocturnal inversion reaches 900 mb (not shown). By 1200 UTC this inversion is eroded in both the model and observations, but the LEM CBL grows more slowly throughout the day, reaching 850 mb (750 mb in the observations) at 1200 UTC, and 620 mb as opposed to 580 mb at BBM at 1500 UTC. In terms of CBL temperatures, the model initially warms faster, but is cooler than observations at the end of the day, although differences are generally less than 0.5 K,

reaching a maximum of 1 K at 1800 UTC. The RL is moister than the CBL, which allows the CBL humidity to increase as it grows between 1200 and 1500 UTC. The final CBL humidity of $4 \, kg \, kg^{-1}$ is consistent between the runs, suggesting there is no large-scale moisture advection during the day. These differences, however, are not expected to have a significant impact on the CBL processes, as the general structure of the Saharan ABL, with a CBL and near-neutral RL separated by a small inversion, is well characterized and representative of the average Saharan ABL profile (Fig. 2a).

The three main mechanisms that the LEM does not represent are large-scale advection, large-scale subsidence, and the impact of dust on the radiation budget. The aerosol optical depth on 20 June 2011 was ~1, as derived from the Cimel sun-photometer at BBM (Marsham et al. 2013b). Dust interacts with both longwave and shortwave radiation, and can contribute to atmospheric heating on the order of a few kelvins per day, while decreasing surface temperatures, although exact heating rates are uncertain and depend on the particle size distribution (Ryder et al. 2013). Depending on whether the dust is located in the CBL or RL, this would help destabilize or stabilize the CBL respectively. Although radiative effects from dust are likely to be dynamically important, their potential impacts on the Saharan ABL are so wide-ranging, that they are beyond the scope of this paper. Large-scale advection of the RL can affect the stability of the CBL. The RL will also be fairly variable in the horizontal (given that the CBL height is variable), so advection at the RL top could contribute to the changes at BBM between 1500 and 1800 UTC at the top of the RL. Changes at the top of the RL due to advection are not represented in the LEM, but given that at the top of the RL there is usually a strong inversion (e.g., Fig. 2a), changes in its height during the day should not affect the turbulent processes below. Finally, large-scale subsidence induces upper-level warming, and is likely to also have an impact on the Saharan ABL structure.

2) MEAN CBL AND RL PROPERTIES

Figure 4 shows the diurnal evolution and horizontal variability of the Saharan ABL in the LEM during the time of quickest CBL growth. Although the surface fluxes and initialization (including the surface tracer) are horizontally homogeneous, there is substantial variability in the CBL depth and tracer concentrations at the horizontal turbulent eddy scale (1–2 times the CBL depth, consistent with the spacing in up and downdrafts; Fig. 4, right panels). Even at 1300 UTC, when the CBL is still relatively shallow, changes in CBL depth of ~100 mb (~1 km) can be observed over short distances

(e.g., between $x = 10$ and 12 km, Fig. 4a). By 1600 UTC this variability has increased to >200 mb (~2.3 km, Fig. 4g). Horizontal variability in CBL height due to turbulence is not surprising, and this would be expected to scale with the CBL height, which in this case is large. However, as discussed in section 3a, the small temperature difference between the CBL and RL, combined with the weak stability within the RL, also plays an important role, as overshooting parcels will travel farther than in a boundary layer with a stronger inversion and stronger RL stability. Evidence for this is also found in the aircraft measurements, where an overshooting plume is observed within the RL rising at $6 \, m \, s^{-1}$ despite being at least 60 mb above the CBL top (Fig. 5, with the plume centered at 1.8 km; see section 3c for a full discussion on the CBL evolution in the aircraft data). The plume is only 0.5 K cooler than the RL; therefore, there is only a very weak buoyancy force that needs to overcome the high initial upward momentum, and the plume temperatures and vertical velocities are consistent with the model (e.g., Fig. 4b, $x = 9$ km or Fig. 4f, $x = 0$ km; potential temperatures not shown). Within the CBL, entrained air from the RL can be carried down nearly undiluted all the way to the surface (not shown, although Fig. 4e shows a plume of only partially diluted entrained air descending as far as 900 mb at $x = 10$ km). As the CBL is continuously growing, thus constantly entraining clean air, the tracer is never well mixed within the CBL, leading to significant horizontal variability in tracer concentrations (Fig. 4, left panels). The large horizontal variability in the model, which has spatially homogeneous surface boundary conditions, shows the extent to which a single atmospheric profile, for example from radiosonde observations, can differ from the average over an area the size of an NWP grid box [an issue that is also discussed for shallower boundary layers in the United States in Weckwerth et al. (1996)]. The interpretation of dust measurements must also take into account the large variability in concentrations that can occur solely by turbulent processes.

CBL variability also controls the formation of clouds. Despite the extremely dry conditions, the large depth of the Saharan ABL means that parcels can still ascend to their lifting condensation level, forming boundary layer clouds, even at around 5-km altitude (Parker et al. 2005). For example, at 1600 UTC, when the CBL has reached its maximum extent, clouds form where the CBL is locally deepest ($x = -9$ km, Figs. 4g,h). By 1700 UTC, cloud cover in the model reaches a maximum value of 4%, consistent with, although on the lower end of, a climatology based on satellite observations (Stein et al. 2011). The conditions in the model here are somewhat drier than the average (cf. Figs. 2 and 3), and the
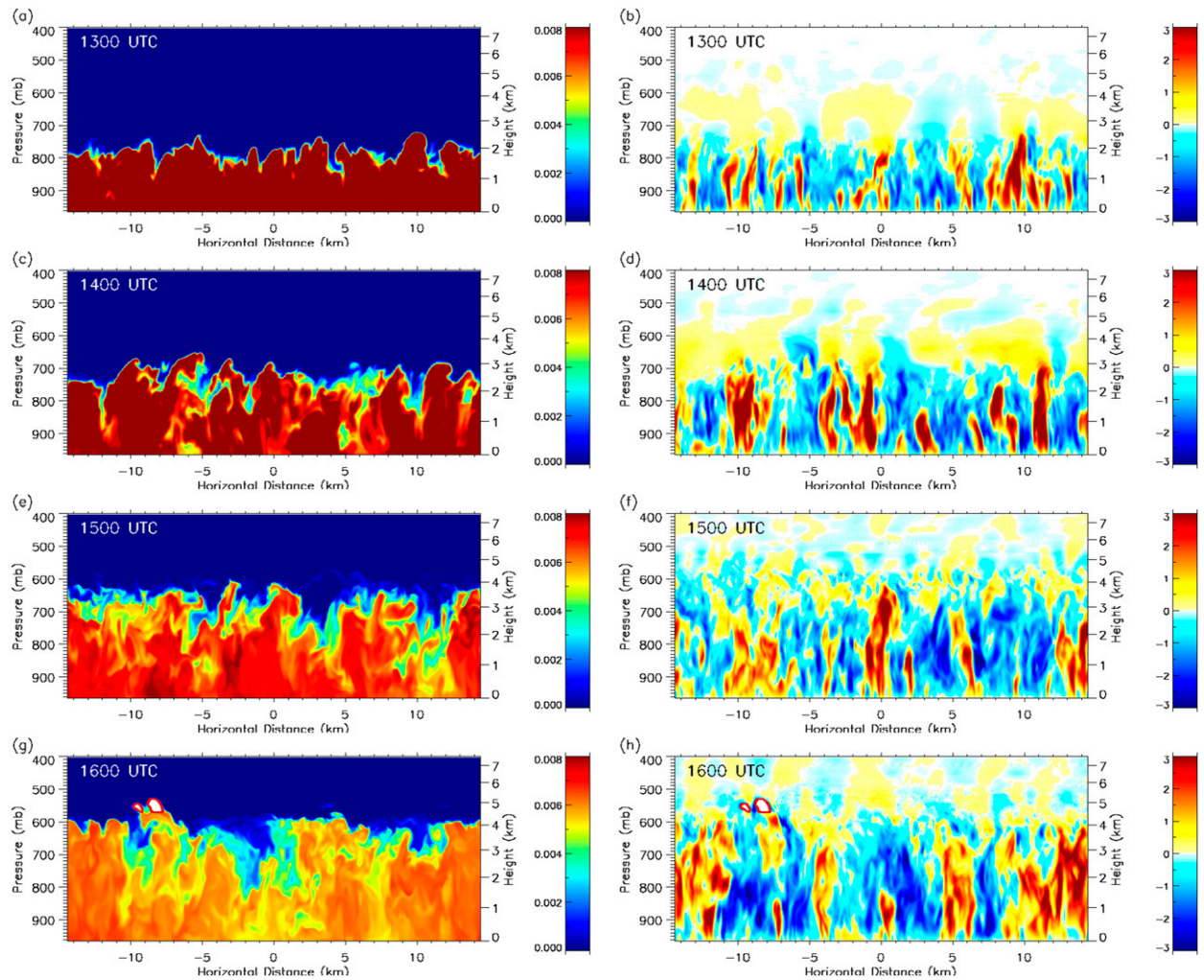
FIG. 4. (a),(c),(e),(g) Contours of a passive tracer initialized at 0900 UTC in the lowest model level and (b),(d),(f),(h) vertical velocity at (top to bottom) 1300, 1400, 1500, and 1600 UTC. Red contour lines filled in white show clouds.

maximum CBL top can be higher than in the LEM simulation, where it reaches 600 mb, which would enable more parcels to reach their lifting condensation level, thus increasing cloud cover. Failure of large-scale models to correctly represent the Saharan ABL will affect not only cloud fractions, but also the timing and duration of Saharan clouds, which in turn affects the radiative budget in the Sahara. Dust and moisture are often associated in the central Sahara (Marsham et al. 2013b), so errors arising from dust and cloud are likely to be coupled. The small depth of these clouds ($\sim$20 mb), much less than a typical NWP vertical grid spacing, coupled with their sensitivity to CBL humidity and the Saharan ABL evolution means that the representation of Saharan clouds in global models is likely to be poor, but the extent of this error and any radiative bias associated with it is currently poorly understood.

One effect of the weak temperature inversion is that CBL plumes are only marginally cooler, sometimes even warmer, than the RL. This allows transport from the CBL to the RL, as plumes can detrain at the CBL top. Although the local CBL top, indicated by the strongest gradient in tracer concentration, can be identified by the transition from the warmer colors to blue in Fig. 4 (left panels), consistent with the vertical velocities (Fig. 4, right panels) and potential temperatures (not shown), significant tracer concentrations can be found above the CBL top in regions where the CBL is locally shallow, for example between $x = -3$ and 0 km at 1600 UTC. Low concentrations of tracer can also be observed above the deepest CBL tops, for example at $x = 5$ km and 580 mb in height at 1500 UTC (in slightly lighter blue than the background), and more such events can be observed in animations of the 2D tracer evolution. Tracer
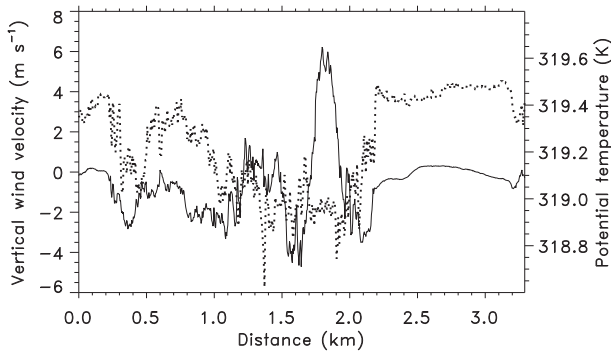
FIG. 5. Vertical velocity (solid line) and potential temperature (dotted line) at 1510 UTC for a single plume measured by the aircraft at 23.89°N, −5.04°E and 620 mb.

concentrations in these plumes are low due to the fact that air is being detrained into a deep, tracer-free RL, and the presence of mixing within the RL quickly dilutes the detrained parcels. Although the impact of detrained plumes on tracer transport is small, their thermodynamic impact, particularly in terms of CBL growth, may be important.

Figure 6 shows probability density functions of potential temperature and vertical velocity anomalies in the CBL and RL. Different methods were used to derive these anomalies in the different datasets, due to differences in the information available. For the LEM, the 3D field was used at 1400 UTC, with the anomalies representing deviations from the horizontal domain mean at each height. Only data above 900 mb were used, to only include the well-mixed portion of the CBL. Tracer concentrations were used to differentiate between the CBL and RL in the LEM data to account for the horizontal variability in CBL height, which is not captured in the other datasets. A test using only the mean CBL height to differentiate the layers in the LEM did not significantly alter the distribution. For the 1200 UTC BBM radiosondes no vertical velocity data were available, and the temperature anomalies were computed as perturbations from the detrended profile to remove the slight stability of the RL and only show the turbulent variability in the data. Finally, the bottom three runs of the aircraft data (960–730 mb, 1352–1434 UTC) were used for the CBL, and the western end of the top two runs for the RL (680–620 mb, 1455–1514 UTC), and the anomalies were computed by high-pass filtering the time series with a 10-km cutoff length scale [see section 3c(1) for more details on the aircraft path]. This removed the impact of any mesoscale variability along the flight track.

Despite the strong surface heating, the distribution of temperatures in the CBL is very narrow, mostly confined to ±0.5 K in all datasets. While the BBM radiosonde data

show a slightly broader distribution, this could be accounted for by slight changes in stability within the RL unaccounted for when detrending the profile. The narrow temperature distribution can be explained by the fact that, due to the small temperature difference between the CBL and RL, entrained air will only be slightly warmer than the CBL air. Eddies due to strong surface heating are also quickly mixed into a very deep CBL, reducing their impact. Finally, detrainment of the hottest plumes from the CBL top will also act to reduce the temperature range within the CBL.

The vertical velocities, on the other hand, are mostly confined to −5 to 5 m s^{-1} for the CBL as a whole, although peak vertical velocities are higher on average close to the CBL top, reaching up to 10 m s^{-1} in the aircraft observations. Again, despite the differences in how the anomalies are computed, the match between the model and aircraft observations is very close, confirming that the model is representing the turbulent characteristics of the Saharan ABL in an appropriate manner.

The RL distribution in temperatures is also relatively narrow. This suggests some degree of mixing within the RL. The presence of significant vertical velocities throughout the RL (±2 m s^{-1}) is consistent with both turbulent mixing and the presence of waves, and results in section 3b(3) show evidence for both processes having a contribution. These vertical velocities are not simply a result of sampling overshooting plumes within an otherwise stable RL, as this would lead to a more discontinuous distribution, with many low vertical velocity events and a few high velocity events. Furthermore, the sampling of the LEM data effectively eliminates overshooting plumes from the distribution. Turbulence in the RL helps maintain the near-neutral state of the layer and could contribute to CBL detrainment, by mixing overshooting plumes into the rest of the RL, preventing them from returning to the CBL.

3) DIURNAL EVOLUTION OF THE CBL AND RL

The diurnal evolution and growth of the CBL is important to understand the characteristics of the Saharan heat low. The growth of the CBL into the RL controls the vertical, and subsequent long-range horizontal, transport of heat, moisture, and mineral dust. Clouds are also a recurrent, albeit poorly understood, feature in the Sahara, and depend critically on the Saharan ABL growing deep enough to reach the lifting condensation level of such a dry atmosphere.

Figure 7 shows profiles of modeled potential temperature profiles and fluxes. Figures 7a and 7b show the "classic" BL flux profile of a warming CBL with fluxes decreasing to a minimum at CBL top, above which the
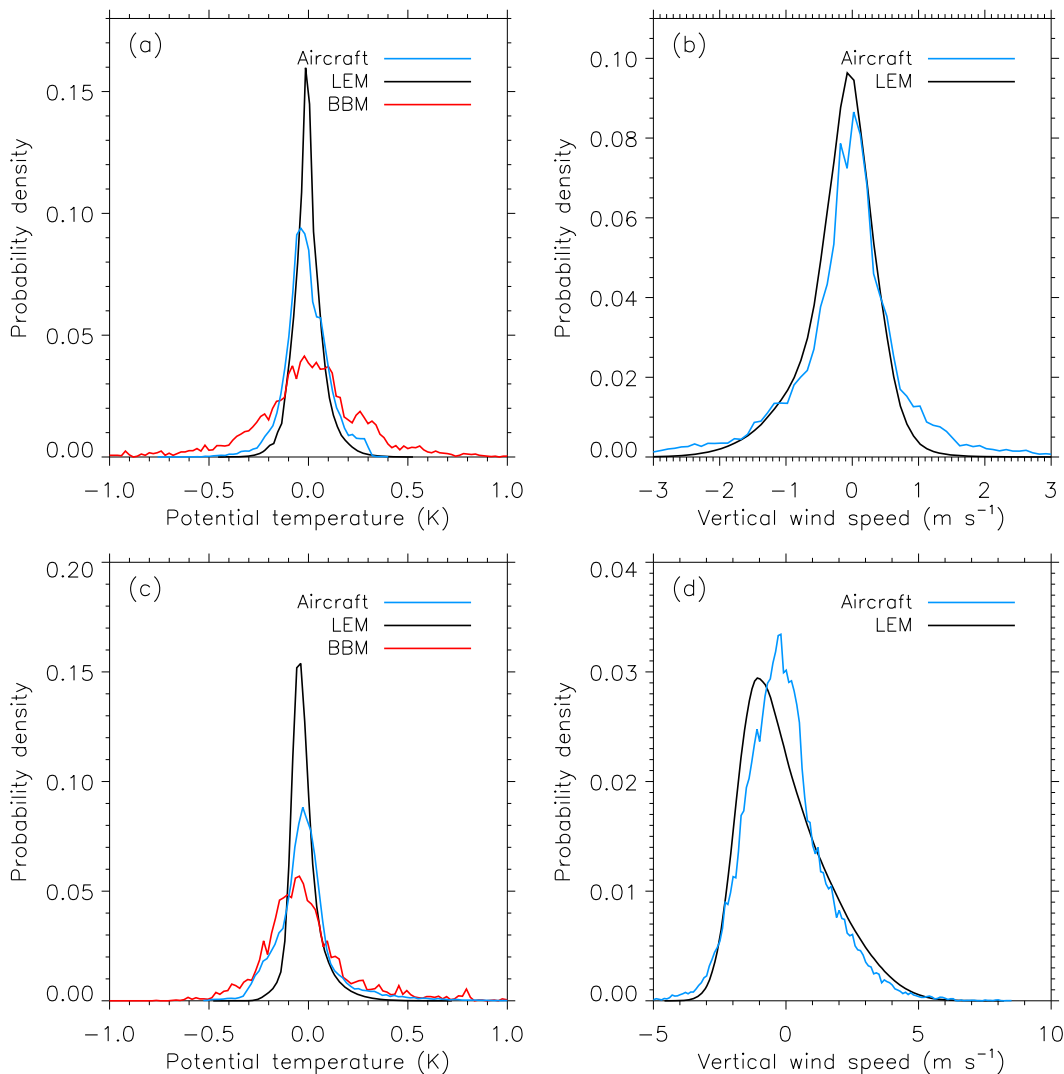
FIG. 6. Probability density function of potential temperature anomaly and vertical velocity in the (a),(b) RL and (c),(d) CBL in the LEM (1400 UTC, black), the BBM radiosondes (1200 UTC, red), and the aircraft observations (1400–1500 UTC, blue).

atmosphere is cooling due to entrainment. At 1200 and 1300 UTC the CBL is growing into a moist RL and the CBL has negative fluxes of humidity and is moistening, with drying of the RL above. By 1600 UTC the CBL is growing into the dry free troposphere (FT) and has positive fluxes of humidity and is drying. At the intermediate times of 1400 and 1500 UTC the flux profile is more complex with two clear minima in the heat flux at 1400 UTC. We discuss this evolution and the processes responsible in this section.

The combination of a weak temperature inversion, deep near-neutral RL and strong sensible heating at the surface should all contribute to a rapid growth of the CBL. In the LEM simulation, however, the CBL completely erodes the RL only by 1600 UTC (Fig. 7e).

Idealized theoretical studies suggest a constant ratio between the entrainment and surface buoyancy flux. More realistic laboratory and large-eddy simulation studies have found the ratio to vary between about 0.1 and 0.2 (Deardorff et al. 1980; Sullivan et al. 1998; Brooks and Fowler 2007) and that the ratio increases with wind shear across the inversion (Moeng and Sullivan 1994; Pino et al. 2003; Conzemius and Fedorovich 2006). Here we find this flux ratio (the ratio between surface fluxes and the minimum in fluxes, found in the entrainment zone) to be substantially smaller than in previous studies, just 0.03, despite the presence of shear at the CBL top, and this reduced entrainment flux is linked to the slow growth of the CBL (Figs. 7a,b). The flux ratio increases throughout the afternoon, only approaching 0.2,
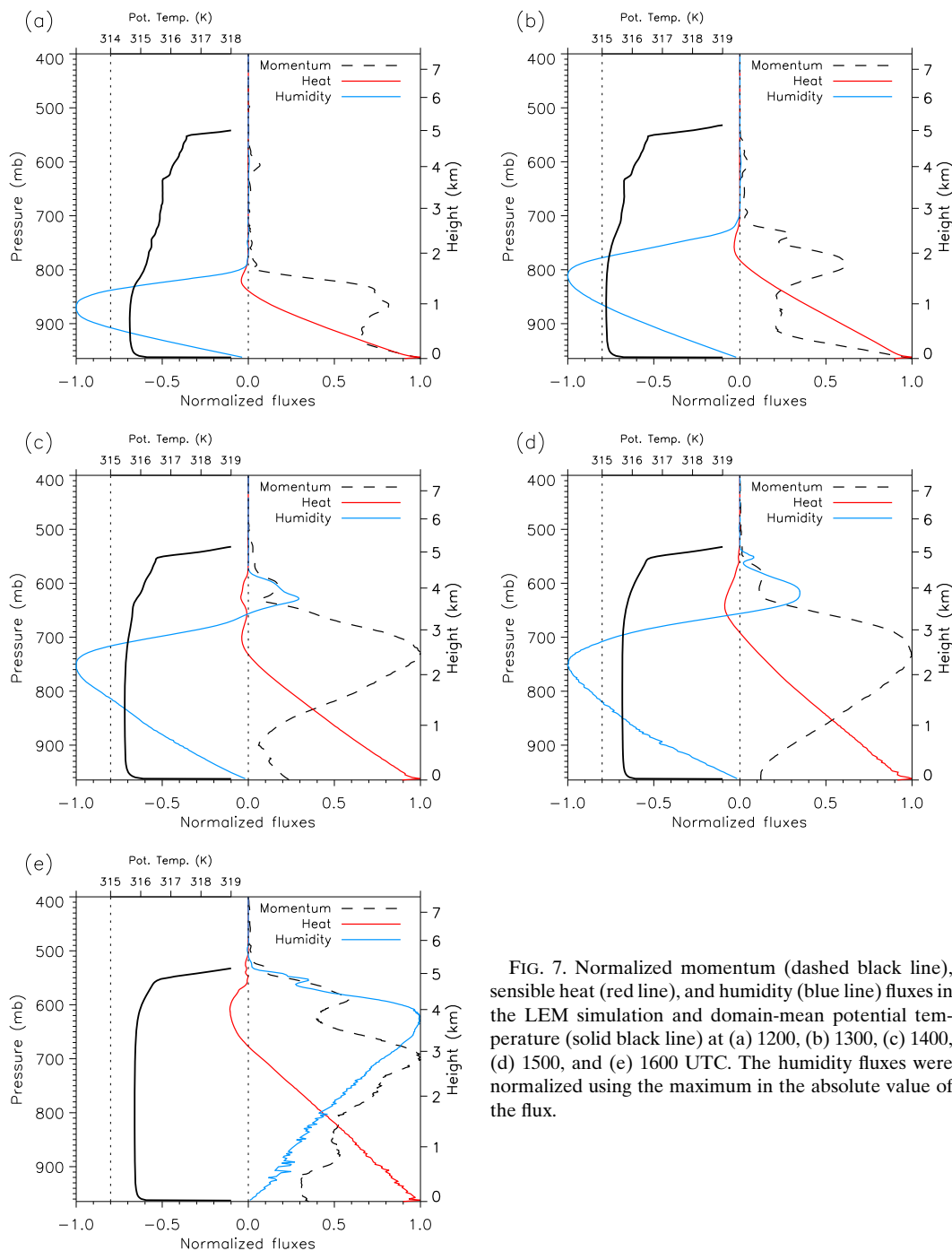
FIG. 7. Normalized momentum (dashed black line), sensible heat (red line), and humidity (blue line) fluxes in the LEM simulation and domain-mean potential temperature (solid black line) at (a) 1200, (b) 1300, (c) 1400, (d) 1500, and (e) 1600 UTC. The humidity fluxes were normalized using the maximum in the absolute value of the flux.

the value typically used by entrainment rate closures in general circulation models, at 1730 UTC (cf. Fig. 13 in section 3d). At this time the CBL has eroded all of the RL, and is therefore capped by the stable, free troposphere, suggesting that the weak entrainment fluxes are associated with the particular structure of the midday Saharan ABL.

Although the CBL deepens via entrainment throughout the day, detrainment of some of the plumes that overshoot into the RL, as shown in section 3b(2), reduces the entrainment rate, slowing the rate of growth. Under strongly convective conditions entrainment typically proceeds via the overshooting of plumes into the inversion or overlying warmer air where they become negatively buoyant and sink back into the boundary layer, bringing some of the overlying air down with them (Sullivan et al. 1998). Here the inversion is weak and the

overlying air only slightly warmer than that in the CBL. The small temperature difference means that convective plumes penetrating into the RL experience little negative buoyancy, even if cooler than the RL air; they may thus penetrate a significant distance, while shear-induced turbulence at the edge of the plume or existing turbulence in the RL may detrain some air from the plume into the RL before it sinks back into the CBL. Some plumes may be warmer than the RL air; these remain positively buoyant in the RL and do not sink back into the CBL. These plumes thus act to remove material from the CBL, reducing the rate of growth by entrainment. They also transfer the warmest parcels of air from the CBL to the RL, acting to reduce the rate of warming of the CBL and to heat the RL; this constitutes a positive heat and buoyancy flux contribution at the top of the CBL, reducing the magnitude of the negative entrainment flux between the two layers. This process acts to maintain the temperature differential between the two layers against the warming of the CBL, reducing the rate at which the inversion is eroded and slowing CBL growth further.

As the CBL grows, overshooting plumes begin to reach the RL top. These can be identified as parcels of nearly undiluted tracer concentrations with associated negative temperature anomalies extending up to 600 mb in height (e.g., at $x = 7$ km in Fig. 9b). These plumes entrain warm, dry free-tropospheric air into the RL, thus increasing CBL detrainment (as the parcel will no longer be negatively buoyant) and also producing a negative heat flux and positive moisture flux at the RL top. This gives rise to the two entrainment zones with two minima in heat fluxes at 1400 UTC (Fig. 7c).The lower zone is where the CBL is growing into the moist RL. The upper zone is in a slightly drier and more stable portion of the RL (650 to 570 hPa). The warming of the RL due to entrainment at the RL top (620 hPa) helps maintain the temperature inversion between the CBL and RL, slowing down CBL growth further. By 1500 UTC there is a single, deep ($\sim$150 mb or 2.4 km) region of negative heat fluxes. At this time, however, the CBL has not completely eroded the RL yet, and two mixing regions remain: one between the CBL and the lower RL (600–670 hPa) and the other at the RL top (530–600 hPa). This is apparent from the moisture flux; at 1200–1300 UTC the moisture flux is negative, as the RL is moister than the CBL (Fig. 3), which leads to a downward transport of moisture as the CBL grows. From 1400 to 1500 UTC moisture fluxes remain negative within the CBL, but become positive above, as dry air is transported downward at the RL top. This is in contrast with 1600 UTC, when moisture fluxes are positive throughout the CBL and the CBL is growing into the FT, coinciding with an increase in entrainment fluxes, which reach 18% of the

surface fluxes at 1730 UTC—this is now consistent with the typical 10%–20% of the surface flux observed by previous studies of entrainment.

At all times, momentum fluxes within the RL are nonzero, demonstrating the presence of turbulent mixing within the RL (Fig. 7, dashed lines). At 1200–1300 UTC these momentum fluxes are relatively weak, with a peak at the top of the RL. Wave patterns in the potential temperature and vertical velocity can also be observed at the RL top [e.g., at $(x, y) = (10, 10)$ and $(-5, -3)$ in Figs. 8a and 8b]. The waves are oriented perpendicular to the mean wind and have length scales on the order of a few hundred meters (longer 5–10-km waves can perhaps be seen, but are much clearer in Fig. 9a 1 h later). These waves are consistent with shear at the RL top, which is a persistent feature of the Saharan ABL (Fig. 2c), generating the momentum flux at this location. As highlighted in Fig. 2b, the conditions in the RL are such that even if turbulence is not generated, it can be maintained; this could potentially allow the impact of shear-induced turbulence to extend downward. The combination of near-neutral conditions and turbulence, albeit weak, in the RL provide a viable mechanism for the mixing out of overshooting CBL plumes.

Later in the afternoon, a wave pattern develops in the potential temperature and vertical velocities, which are 90° out of phase (Fig. 9a), of larger magnitude and wavelength (on the order of $\sim$5–10 km) to the waves observed at 1300 UTC (Fig. 8). Plumes that penetrate the RL, without reaching the top (as shown by the tracer concentrations at 665 mb, Fig. 9a) line up with the cold temperature anomalies aloft and lie between the positive and negative vertical velocity anomalies (e.g., at $x = -1$ and 2 km, Fig. 9b). This indicates that overshooting plumes also generate waves within the RL. The large spread in vertical velocities in the RL (Fig. 6b) can therefore be associated partly with these waves and partly with the turbulent fluxes in the RL associated with shear-induced mixing and CBL plumes overshooting the RL top. The presence of waves in the RL, and entrainment at the RL top, has also been observed in lidar measurements over Paris (Fochesatto et al. 2001).

In summary, in the afternoon, at the time of most rapid CBL growth, there are two possible fates for rising plumes: the coolest CBL plumes entrain RL air, contributing to CBL warming and growth, and the warmest plumes detrain into the RL. This reduces the entrainment flux at the CBL top, contributes to turbulent mixing within the RL, and generates waves that increase the variability of potential temperature and vertical velocity at the RL top. Later in the afternoon, the CBL is deep enough that detrained plumes also warm the RL by entraining free-tropospheric air, producing a heat flux
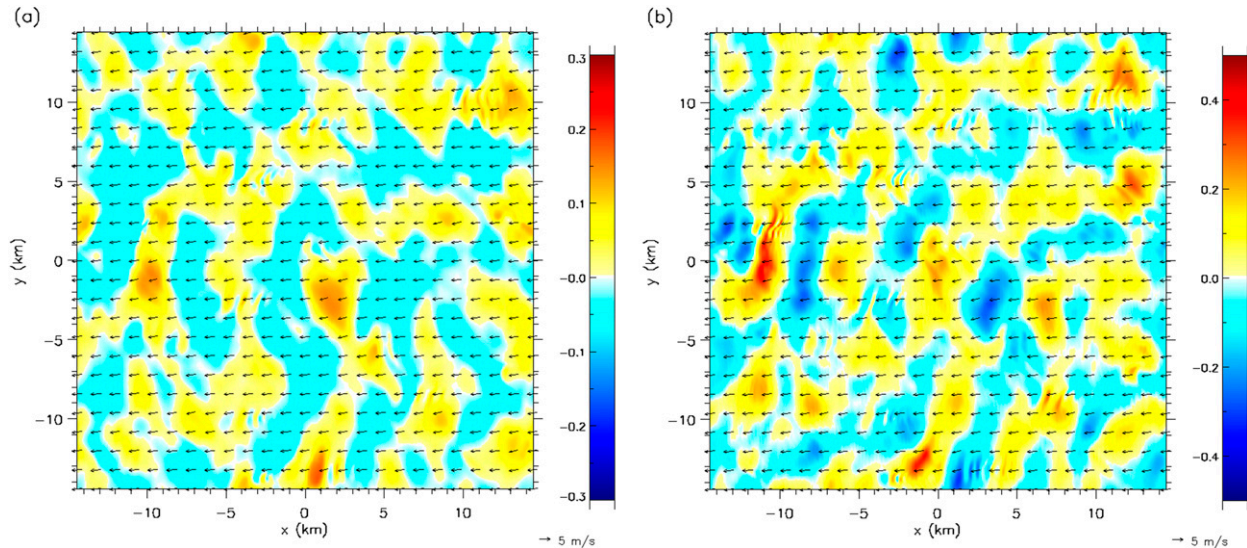
FIG. 8. LEM 1300 UTC (a) potential temperature perturbation from the horizontal mean and (b) vertical velocity, with horizontal wind vectors, at 630 mb.

profile with two entrainment zones. Overall, this means that while CBL detrainment can only occur due to the presence of a weak temperature inversion, it also acts to maintain the inversion. Weakened entrainment also slows down CBL growth, and may contribute to the Saharan ABL not reaching its maximum extent until late in the afternoon despite the presence of both strong surface heating and a very weak temperature inversion, as found in observations (Fig. 2; Cuesta et al. 2008; Marsham et al. 2013b).

c. Aircraft observations of the Saharan ABL

1) OVERVIEW OF AIRCRAFT OBSERVATIONS

The aircraft case study took place on 12 June 2012 and aimed to sample the vertical structure of the boundary layer in northern Mali, as close to the Saharan heat low as the aircraft range permitted and where the CBL was forecast to be hot and deep (white line, Fig. 1). The east–west track ($-5.4°$ to $-4.4°$E) was first overflown at high altitude, and two Vaisala RD94 dropsondes were launched at either end (Fig. 10, black lines) before descending to minimum safe altitude (~80 m above ground level). During the descent the aircraft traveled eastward to $-4°$E and 550 mb in height and then turned around completing the descent westward to the western end of the bottom run in Fig. 10. The dropsondes were used to identify the heights at which to fly the subsequent legs so that they would best capture the layers of interest in the Saharan ABL. The dropsondes were launched at 1313 and 1320 UTC, with the stacked legs taking place between 1352 (start of lowest leg) and

1514 UTC (end of the uppermost leg in Fig. 10). The aircraft then ascended westward from the western end of the uppermost run.

The track was characterized by a synoptic low-level temperature gradient with lower pressures in the east, which is consistent with the albedo gradient along the flight path (decreasing west to east, not shown), although the pressure gradient may also be due to synoptic temperature changes in the heat-low region. The dropsonde profiles are consistent with the low-level temperatures, with a warmer and deeper CBL in the east, reaching 770 mb, compared to the west where it reached 820 mb, and RL heights of 520 and 540 mb respectively. The temperature difference across the CBL top in both cases was <1 K, but the water vapor mixing ratio and wind profiles (not shown) confirm that this weak lid was acting as a capping inversion. Lidar data were used to estimate the CBL height along the track, by visually inspecting each single lidar profile and subjectively identifying a discontinuity in the gradient of the backscatter with height (stars and dashed line in Fig. 10). The lidar captures the large variability in CBL depths at the horizontal turbulent eddy scale, with a change of >100 mb between $x = 20$ and 25 km, consistent with the LEM. At the mesoscale, the lidar-derived CBL height is consistent with the low-level temperatures, showing deeper boundary layers in the east, with a fairly distinct transition at 60 km (4.9°W).

The presence of a transition between two boundary layer heights is confirmed in the in situ aircraft measurements taken just under 2 h later. The two highest runs (at 680 and 620 mb) show mostly laminar conditions for
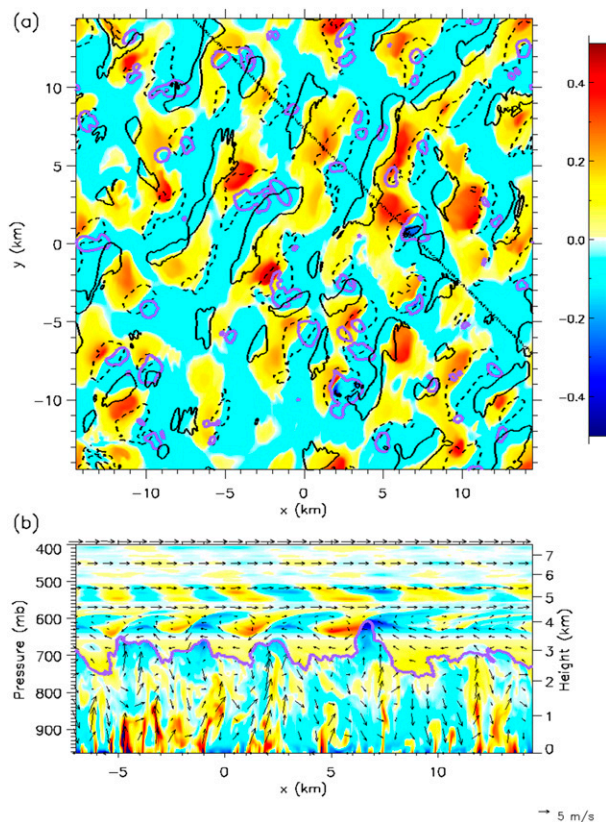
FIG. 9. (a) LEM 1400 UTC potential temperature anomaly from the horizontal mean (color contours) and vertical velocity (-0.5 and $0.5\,\mathrm{m\,s^{-1}}$ for the black dashed and solid black lines, respectively) at 630 mb, and tracer concentrations at 665 mb (thick, purple contours). The different heights are used to highlight the impact of plumes (shown by the tracer concentrations) on the air directly above. (b) As in (a), but along an x–z transect perpendicular to the wave pattern [dotted line in (a)], with wind vectors overplotted (vertical velocity contours are omitted).

FIG. 10. Aircraft track contoured with virtual potential temperature. The track shown extends from 24.0°N, -5.4°E ($x = 0$ km) to 23.7°N, -4.4°E (see also the white line in Fig. 1). Measurements cover the period from 1352 UTC (start of the lowest leg) to 1514 UTC (end of the uppermost leg). The potential temperature profiles from the two dropsondes launched before the descent (at 1313 and 1320 UTC) are overplotted in black, with the vertical dotted lines indicating their location. The dashed line shows the CBL height as derived from the onboard lidar. The vertical dash-dotted line shows the boundary for the "east" and "west" portions used in the analysis.

$x < 60$ km, with low values of $\overline{w'\theta'}$, except for a few bursts in turbulence due to overshooting plumes (e.g., at $x = 40$ km in Fig. 11b, which is the plume shown in more detail in Fig. 5). In the eastern section of the flight track the high values of $\overline{w'\theta'}$ are indicative of active turbulence. These results suggest that, at this time, when $x < 60$ km (i.e., the eastern section) was within the CBL, while the CBL top in the west was below 680 mb, with the aircraft flying within the RL above this height. The eastern and western portions of the track were therefore considered separately in the rest of the analysis (with the boundary given by the vertical dash-dotted line in Fig. 10).

2) SAHARAN ABL STRUCTURE AND EVOLUTION AS OBSERVED IN AIRCRAFT DATA

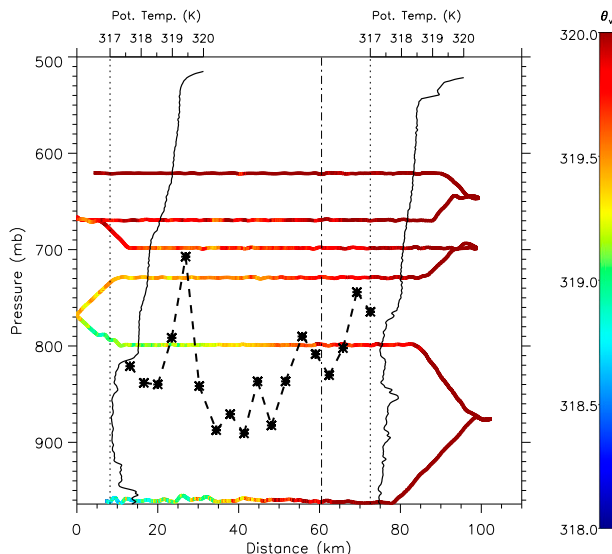Interpretation of the aircraft data is made difficult due to the time evolution of the Saharan ABL throughout the flight. Although the Saharan ABL was sampled at a variety of heights, aimed to capture the CBL and RL, it is, for the most part, impossible to ascertain definitely from the in situ data how the different layers evolve during the flight and so where the aircraft is flying at any given time relative to the CBL and RL tops. Although it is difficult to gain an overarching understanding of the Saharan ABL from the aircraft observations alone, it is possible, however, to find evidence for some of the boundary layer processes described with the model data.

Turbulent fluxes can be computed for each level run from the aircraft data using the eddy covariance technique. The eastern and western portions of the flight track were considered separately (Fig. 12, stars and crosses respectively). On these level runs, anomalies were computed by high-pass filtering the data with a 10-km length-scale cutoff in order to remove any mesoscale variability in the data. The aircraft profiles (descending to minimum altitude and ascending away from the study region, not shown in Fig. 10) were at a very shallow angle (2%–4%), which also allowed the computation of turbulent fluxes as a function of height, in this case using short averaging lengths, as in Brooks et al. (2003) (Fig. 12, lines). The high-pass-filtered profile was used, with a 5-km cutoff, to remove any vertical
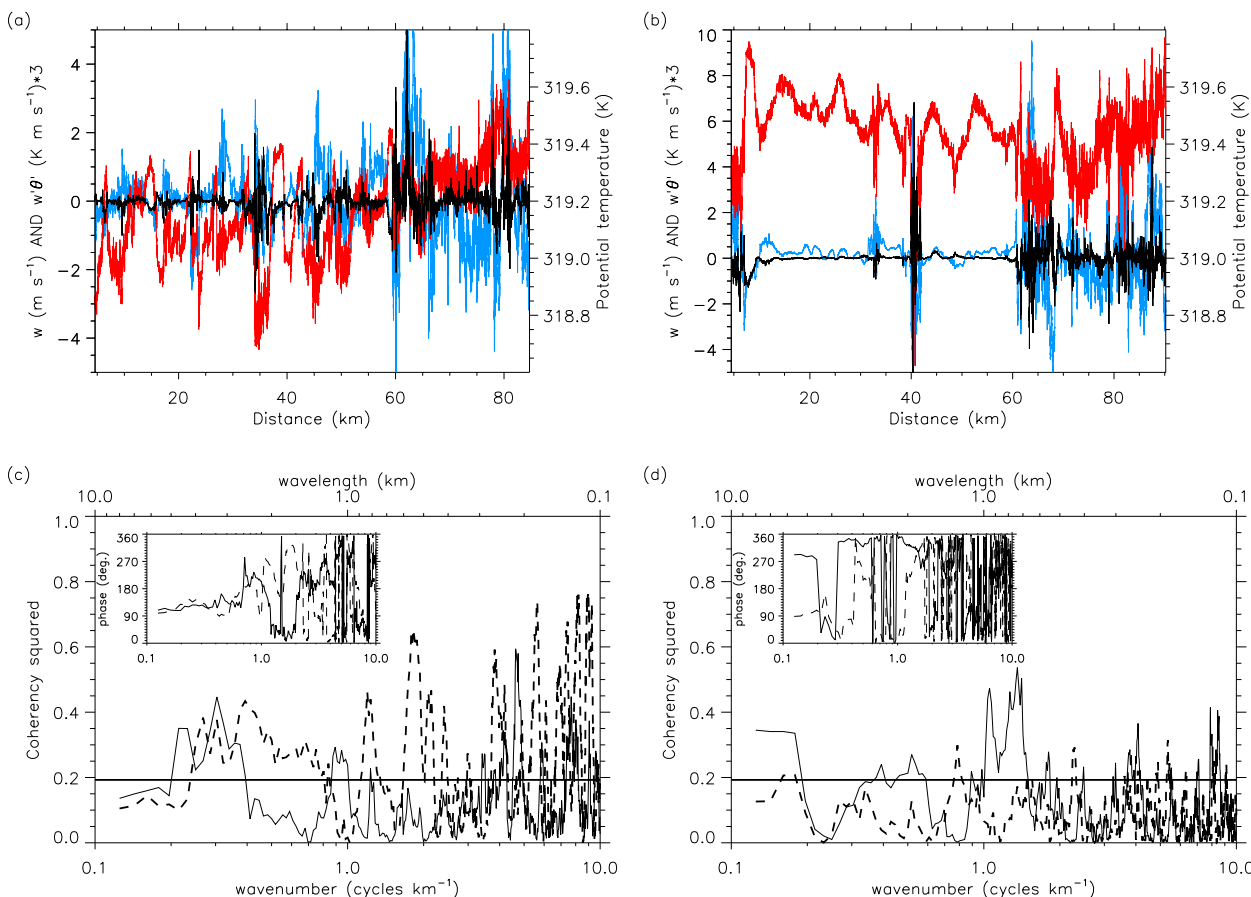
FIG. 11. (a),(b) Aircraft observations of vertical velocity (blue line), potential temperature (red line), and the product of the vertical velocity and potential temperature perturbations (black line) at (a) 680 and (b) 620 mb. Anomalies were computed as deviations from the time series with a 10-km high-pass filter applied. Also shown is coherency squared as a function of length scale for potential temperature and vertical velocity at 680 (solid line) and 620 mb (dashed line) for data where (c) $x < 60$ km (west of $-4.85°E$) and (d) $x > 60$ km (east of $-4.85°E$). The horizontal solid line indicates the 95% significance level. The insets show the phase functions for these pairs of measurements.

variability in the data. The averaging of the anomalies to calculate the fluxes was performed with a 10-km running mean (200–400-m change in altitude), thus minimizing the effect of changing altitude on fluxes. On the descent, the east–west boundary (at $x = 60$ km) was crossed while the aircraft was at 840 mb. The advantage of using the aircraft profiles is that there is little time evolution between the measurements made at each height within a single profile. For the descent the layers can be identified using the dropsonde data, and at this earlier time the aircraft crosses a large portion of the RL. On the other hand, the shorter averaging length used, compared with the flux calculations performed for the level runs, introduces some noise to the flux estimates and the measurements are affected by horizontal variability in CBL properties, which can be considerable over short distances as can be seen in Fig. 10.

The level runs show higher surface heat fluxes in the warmer, eastern portion of the flight track, leading to

a deeper CBL (Fig. 12a). The top leg is still within the CBL in the east, but is in the entrainment zone in the west, consistent with what was expected by inspecting the in situ data directly (Figs. 10a,b). Although the low-level temperature difference between the two sections is only 1.5 K, there is a large change in surface fluxes from 240 to 330 W m^{-2}. The entrainment zone fluxes are only a small fraction of the surface fluxes (7%), also consistent with the weak entrainment observed in Fig. 7, which appears to be a characteristic feature of the Saharan ABL. The heat fluxes near the surface calculated using the downward profile match the fluxes from the level run in the west, providing some validation for the methods used. The magnitude of the profile fluxes at higher altitudes in the CBL is similar to, but slightly smaller than, those calculated with the level runs, consistent with the measurements being taken earlier in the day. Fluxes are positive up to 750 mb, which implies that the CBL heights along the descent varied between 850 mb
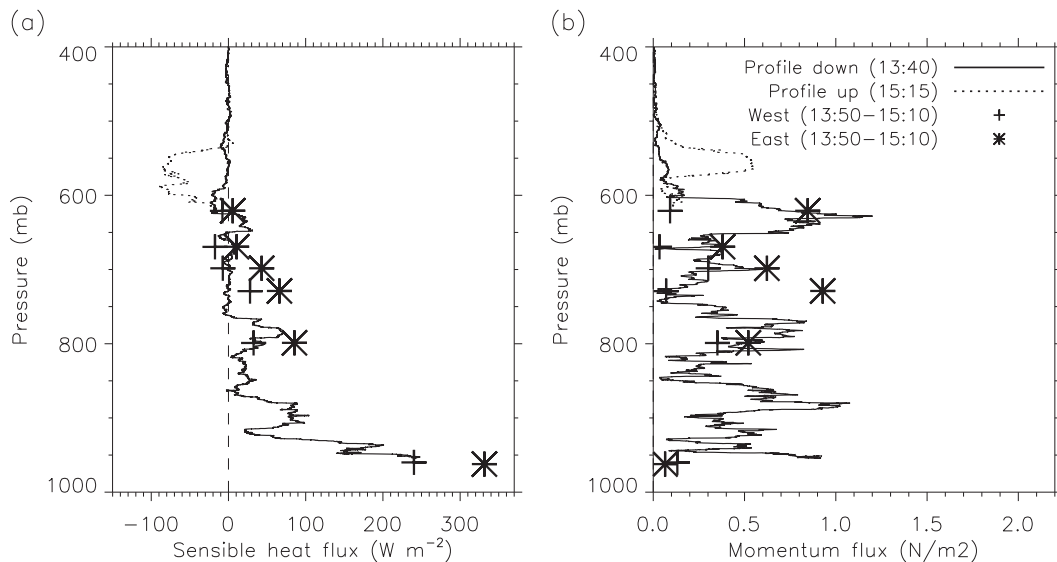
FIG. 12. (a) Sensible heat fluxes and (b) momentum fluxes calculated using the eddy covariance method for each level leg of the aircraft case, split between the western (crosses) and eastern (stars) sections of the track, and using the descent into the study area (solid line) and ascent away from the study area (dotted line). The boundary between the east and west portions was at −4.85°E.

(as seen in the first dropsonde) and just above 750 mb, consistent with the lidar measurements (Fig. 10) and the variability in the LEM simulation (e.g., Fig. 4a).

Momentum fluxes are positive below 550 mb during the aircraft descent, indicating the presence of turbulence within the RL (Fig. 12b, solid line). There is a maximum in momentum fluxes at 625 mb. This is lower than the RL top as seen in the dropsondes, but may correspond to the RL top at the aircraft location: at this height the aircraft is flying outside the track shown in Fig. 10. The momentum fluxes are consistent with the LEM simulation, which showed shear-induced mixing at the RL top, and there is a weak minimum in sensible heat fluxes of −20 W m^{-2} at the same height. During the ascent out of the study region later in the afternoon, the aircraft crosses a region with negative sensible heat fluxes and a peak in momentum fluxes between 610 and 530 mb, showing the presence of an entrainment zone. The aircraft potential temperature measurements show an inversion at 500 mb, and a drop-sonde launched slightly later, when the aircraft was flying at 420 mb, also shows a well-mixed CBL up to 520 mb (not shown). This entrainment zone therefore appears to correspond to the CBL top once it has completely eroded the RL. The higher magnitude of the fluxes compared to the level legs, where the CBL is still growing, is consistent with the LEM results (Fig. 7), with weak entrainment fluxes while the CBL is capped by a small temperature inversion and a deep RL, whereas entrainment fluxes increase once the RL is completely eroded and the CBL is capped by the stable free troposphere.

Within the RL there is variability in potential temperatures and vertical velocity of similar length scale and magnitude to the waves induced by overshooting plumes described in Fig. 9, although the length scale is also consistent with the size of turbulent eddies in the Saharan ABL (Figs. 11a,b, western section). Spectral analysis outlined in Matthews and Madden (2000) was used to determine the spectral coherency (which can be considered as the spectral equivalent to the correlation between two datasets) and the phase difference as a function of length scale between potential temperature and vertical velocity. The analysis was applied separately to the western (Fig. 11c) and eastern (Fig. 11d) sections of the flight track. Within the RL (i.e., in the west) potential temperature and vertical velocity covary significantly at scales of 1–6 km (Fig. 11c), which agrees with the variability observed directly in Fig. 11a. As in the LEM (Fig. 9), the phase shift between these two quantities in the observations is ~90° (inset in Fig. 11c), consistent with waves, generated by plumes. Within the CBL the presence of these waves is much less clear as turbulent mixing dominates the variability in temperature and winds, although there is a small peak in coherency at 680 mb for length scales above 6 km, with a phase shift of 270° (Fig. 11d, solid line).

The aircraft observations are consistent overall with the processes described with the model results in section 3b. The dropsondes launched between 1300 and 1330 UTC show the same overall structure as the radiosonde data (Fig. 2a), with a CBL height of ~800 mb, and

a temperature inversion of <1 K. Along part of the flight track this inversion is not eroded by 1500 UTC. Fluxes measured in the entrainment zone were weak, and positive momentum fluxes, as well as waves, were measured throughout the RL, consistent with boundary layer detrainment affecting entrainment and boundary layer growth, as described in section 3b(3). Once the observed CBL reached the FT the entrainment fluxes increased, consistent with the LEM.

d. Representation of the Saharan ABL in larger-scale models

In section 1 we described the significance of the Saharan ABL for the correct representation of the dynamics and thermodynamics of the large-scale Saharan heat low, as well as the transport of mineral dust. The results in this study highlight the importance of the detailed structure of the Saharan ABL in controlling its variability and diurnal evolution, in particular small-scale features such as the small temperature inversion, and shear-induced mixing at the RL top. The LEM was run with a high vertical (10–35 m below the RL top) and temporal (on the order of seconds) resolution in order to accurately capture these processes. The coarse vertical resolution of operational numerical weather prediction and climate models, particularly at the higher altitudes that the Saharan CBL top can reach, are likely to struggle to capture many of the processes described here. Couvreux et al. (2014) simulated the diurnal cycle in the semiarid region of the Sahel and found that, even with a vertical grid finer than 100 m, their SCM failed to reproduce the fine vertical structure that separated the boundary layer from an overlying layer of Saharan air. Global configurations of the Met Office Unified Model use a time step from 10 to 20 min, depending on horizontal resolution, which may also create problems if the atmospheric profiles change significantly over this time period, for example as a result of the strong surface heating. To evaluate the ability of large-scale models to represent the evolution of the Saharan ABL, the Met Office Unified Model was run as an SCM with the same initial conditions and surface fluxes as the LEM. The SCM was run with two different time steps: 15 min, representing a typical operational value, and 1 min. The vertical grid from the operational global configurations is used, with 62 levels, and two finer grids with 70 and 140 levels were also tested, both with a 1-min time step.

Overall the SCM could be argued to perform reasonably well, with temperature differences compared to the LEM simulation less than a few tenths of a degree (Figs. 13a,b). Given the surface heat fluxes are specified, however, this is perhaps not too surprising. Interestingly, the SCM shows much more sensitivity to time step with

62 levels (Fig. 13a) than it does to vertical resolution at a fixed time step (Fig. 13b). This can also be seen in the time evolution of the CBL depth (Fig. 13c), defined as the height of the minimum heat flux for the LEM and the inversion base for the SCM. The jump in CBL height in the LEM at 1430 UTC is due to the merging of the two entrainment zones (as seen in Fig. 7c), and so an overestimate of the actual CBL top. The SCM shows too rapid growth during the morning, especially early on with the shorter time step, and by 1400 UTC leads to a CBL that is too deep by around 90 mb for all SCM simulations. One potential reason for this rapid growth is the lack of a representation of detrainment into the RL in the SCM, as reflected by the overestimation of the flux ratio, which would otherwise cool the CBL relative to the air above and slow its growth (Fig. 13d). During the growth phase of the CBL (up to around 1400 UTC) the flux ratios for the SCM mostly lie between 0.1 and 0.3, consistent with previous studies of entrainment for boundary layers capped by strong inversions. For the LEM the ratio is consistently less than 0.05 for the reasons discussed in section 3b(3). Where the SCM entrainment fluxes are weaker, especially when a longer time step is used, this is not due to a correct representation of PBL processes, but due to the difficulty in representing entrainment with such weak inversions. The entrainment flux is parameterized through a diffusion coefficient, calculated to give the desired flux from start-of-time step fields (Lock et al. 2000). The flux ratio is systematically lower with a 15-min time step, then, because reductions in the strength of the temperature inversion within the time step lead to weaker entrainment fluxes than the entrainment formula used might suggest. Weak entrainment when using a 1-min time step, on the other hand, is mainly restricted to the period 1400–1430 UTC and is due to the very low lapse rates directly above the temperature inversion at this time. The rapid changes in the flux ratio in these simulations also highlight the sensitivity of the SCM to small changes at the inversion as the CBL grows through the RL, due to the weak stability there.

The SCM also struggles to reproduce the evolution of the vertical structure of the Saharan ABL, with the potential temperature profile being too stable before 1400 UTC, and too unstable afterward (Fig. 13a). The vertical structure is slightly improved with the shorter time step, making it more well mixed, which again suggests that the profile is evolving rapidly relative to the time step, leading to a temperature profile which is too diffuse.

Another shortcoming of the SCM is its failure to produce any cloud throughout the simulation because the mean relative humidity in the grid box never exceeds the
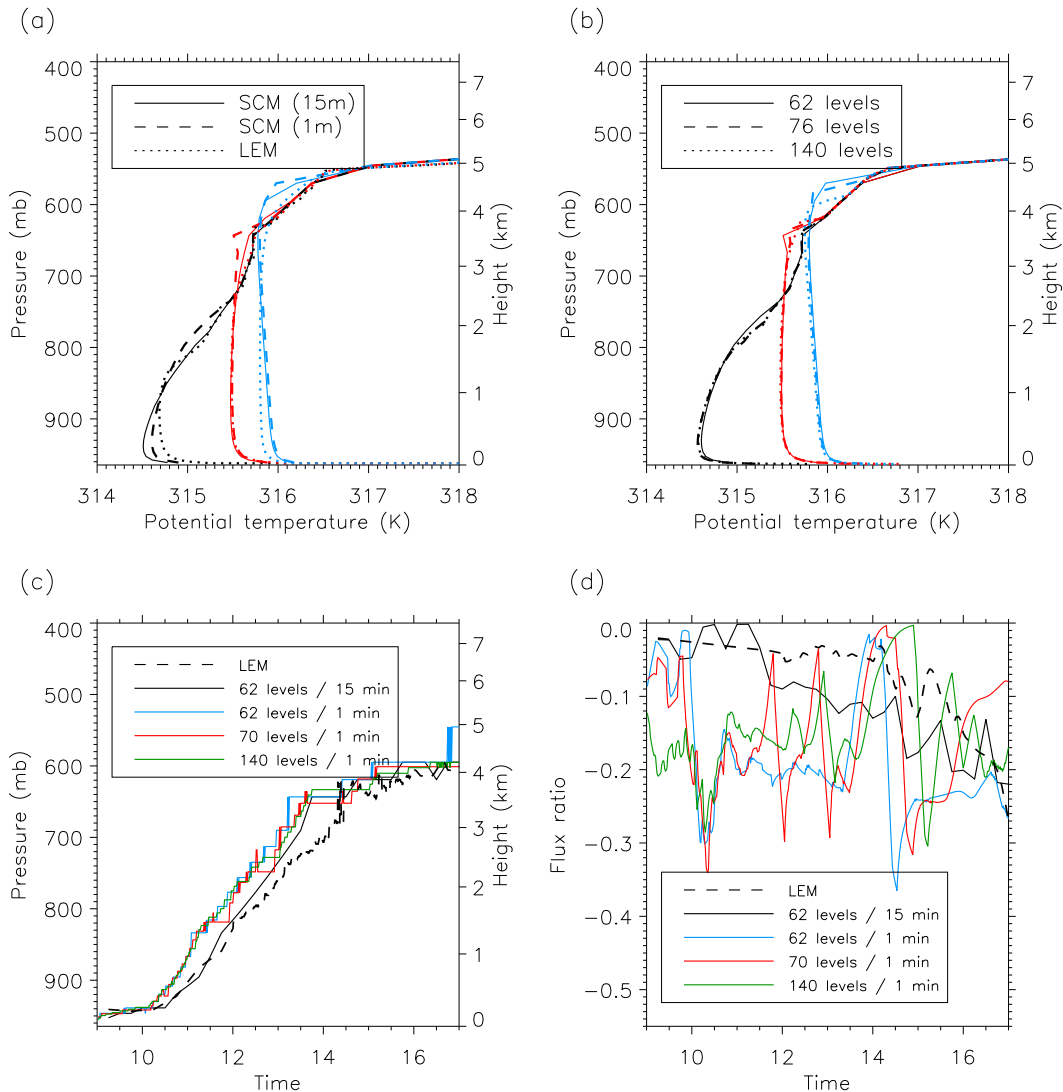
FIG. 13. (a) Potential temperature in the Unified Model SCM using a 15-min time step (solid line) and a 1-min time step (dashed line) and in the LEM (dotted line) and (b) potential temperature in the SCM with a 1-min time step and 62 (solid), 70 (dashed), and 140 (dotted) vertical levels at 1200 UTC (black), 1400 UTC (red), and 1600 UTC (blue). Also shown are the (c) boundary layer height and (d) flux ratio in the five simulations.

critical value of 80%. This is in contrast with the LEM, where clouds are formed in the areas where the CBL is deepest. The SCM (and large-scale models more generally, given their coarse horizontal resolution) do not represent the large CBL variability at scales of 5–10 km that is observed, which provides the mechanism to bring parcels to their lifting condensation level. Errors in cloud cover can have a large impact on the radiation budget, although more work is needed to understand the relative importance of different forcings, such as clouds and dust, on large-scale biases in the Sahara.

In summary, the SCM struggles to reproduce the typical three-layer potential temperature structure of the Saharan ABL, with a well-mixed CBL, weak inversion,

and weakly stable RL. Owing to the coarse vertical and temporal resolution, it cannot represent such a small temperature inversion (in terms both of magnitude and vertical extent), and therefore smooths the entire profile. CBL growth is faster compared to the LEM, suggesting that the lack of a representation of detrainment in the SCM is having a significant impact. While clouds are present in the LEM simulation, the SCM fails to trigger the cloud or convection parameterizations at all. While here we provide a quick overview of potential problems in the representation of the Saharan ABL in large-scale models given the insight provided by the LEM results, a more in-depth analysis of these results will provide the basis for future work.

4. Conclusions

A large-eddy simulation model and aircraft and radiosonde measurements made for the first time in the remote Sahara have been used to describe the vertical structure and diurnal evolution of the Saharan ABL. A schematic summarizing the key features and processes identified with both observations and the LEM is shown in Fig. 14. The mean midday Saharan ABL profile derived from radiosonde observations is characterized by a well-mixed convective boundary layer capped by a small (<1 K) temperature inversion at approximately 820 mb, and a deep, near-neutral (lapse rate = 1 K km^{-1}) residual layer that typically reaches 550 mb. The large depth of the Saharan convective boundary layer produces a large variability in CBL depths (up to 2 km over short distances) and in the concentration of a passive tracer in the LEM, despite the spatially homogeneous initial conditions and surface forcing; similar variations were observed in CBL heights derived from the aircraft lidar. This large variability in CBL properties solely due to turbulent processes means that caution must be used in the interpretation of radiosonde profiles of the Saharan ABL, as any individual profile is unlikely to be completely representative of the wider region. This sampling problem could contribute to existing biases in analyses of the Saharan region, given the scarcity of radiosondes being assimilated by operational systems. Turbulent processes can also produce significant variability in boundary layer aerosol, such as dust, even in areas with horizontally homogeneous emissions.

The mean properties of the CBL in the LEM agree closely with both radiosonde and aircraft observations. While the strong surface heating leads to a broad distribution of vertical velocities of -5 to 5 m s^{-1}, with peaks of 10 m s^{-1} at the CBL top, the potential temperatures are confined to ± 0.5 K of the CBL mean. In the residual layer (RL), where the turbulent state is either dominated by shear ($0 < Ri < 0.25$) or indeterminate ($0.25 < Ri < 1$), significant vertical velocities are also measured (± 2 m s^{-1}). These are due to a combination of externally imposed turbulence and waves from overshooting plumes, as well as shear-induced turbulence at the RL top, which produce positive momentum fluxes and turbulent mixing within the RL.

Despite the strong surface heating and small capping inversion at the CBL top, entrainment rates in the Saharan CBL are weak, leading to a slow CBL growth that does not erode the RL completely until late afternoon in both the LEM and observations. A passive tracer introduced in the CBL in the LEM simulation shows the presence of detrainment at the CBL top. The temperature
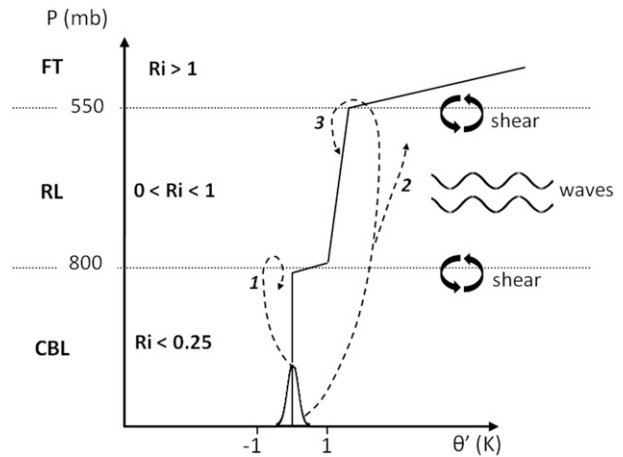

FIG. 14. Schematic describing the main features of the Saharan ABL and the fate of overshooting parcels as the CBL grows. The bell-shaped curve describes the distribution of temperatures in the CBL, and the dashed lines show the fate of plumes of different temperatures as follows. 1) Cooler CBL plumes entrain RL air into the CBL, contributing to CBL warming and growth. 2) Warmer CBL plumes are detrained, as their temperature is similar to the RL and mixing within the RL from shear contributes to mixing them out. This cools the CBL and slows down CBL growth. 3) As the CBL grows, some plumes reach the RL top, entraining free-tropospheric air into the RL. This schematic provides a 1D view of the key processes occurring within the Saharan ABL. In reality, turbulent processes also produce a horizontal variability in CBL depths of up to 50% of the total over horizontal distances on the order of the CBL height.

deficits of the warmest CBL plumes overshooting into the RL are very small, which combined with the presence of some turbulence within the RL allows these plumes to detrain from the CBL top. Detrainment reduces the entrainment rate via the physical loss of material across the interface, and reduces the entrainment fluxes to only 3% of the surface fluxes. As only the warmest plumes detrain, their negative heat flux contribution is smaller than if they entrained RL air and returned to the CBL, and the average CBL temperature is reduced, thus further slowing down the erosion of the temperature inversion. As the CBL grows, detrained plumes can reach the RL top where they entrain free-tropospheric air into the RL, thus producing a second entrainment zone at the RL top. This second zone of entrainment warms the RL, helping maintain the temperature inversion between the CBL and RL even longer and inhibiting CBL growth further. These processes are particular to the Sahara, and possibly other deep, dry desert boundary layers.

The Sahara is a major source of uncertainty in forecast models (Agustí-Panareda et al. 2010; Garcia-Carreras et al. 2013). The particular structure of the Saharan ABL, and in particular the small temperature inversion and deep near-neutral residual layer, directly impact its dynamics and diurnal evolution. The Met

Office Unified Model, run as a single-column model, driven by the same data as the LEM simulation, produces too rapid a boundary layer growth with no cloud formation, highlighting the difficulties of large-scale models in representing key processes in the Saharan ABL, due to their coarse vertical and time resolution. While here we present only a quick overview of the SCM performance, a more detailed analysis of the process-based representation of the Saharan ABL in large-scale models should be the focus of future work. The model errors shown here have direct implications for the representation of a number of important processes in the Sahara in numerical weather prediction models in general. The influx of cool, moist air at low levels from the Atlantic to the west, and from propagating cold pools in the north and south affects the large-scale structure of the Saharan heat low (Todd et al. 2013; Marsham et al. 2013a,b; Garcia-Carreras et al. 2013), and the Saharan ABL controls the vertical redistribution and long-term fate of this moisture. The large depth of the Saharan ABL can lead to the formation of boundary layer clouds despite the dry environment, and their radiative impact depends on the growth, and final depth, of the CBL. Finally, the ability to explicitly simulate dust emissions depends on the correct representation of near-surface gustiness, which depends on CBL turbulence and the downward mixing of upper-level momentum, and dust radiative impacts are also determined by its vertical, and subsequent long-range, transport. The additional impact of mineral dust on boundary layer dynamics is not explored in this study, and should be considered in future research.

REFERENCES

Agustí-Panareda, A., A. Beljaars, C. Cardinali, and I. Genkova, 2010: Impacts of assimilating AMMA soundings on ECMWF analyses and forecasts. *Wea. Forecasting,* **25,** 1142–1160, doi:10.1175/2010WAF2222370.1.

Birch, C. E., D. J. Parker, J. H. Marsham, and G. M. Devine, 2012: The effect of orography and surface albedo on stratification in the summertime Saharan boundary layer: Dynamics and implications for dust transport. *J. Geophys. Res.,* **117,** D05105, doi:10.1029/2011JD015965.

Brooks, I. M., and A. M. Fowler, 2007: New measure of entrainment zone structure. *Geophys. Res. Lett.,* **34,** L16808, doi:10.1029/2007GL030958.

——, S. Söderberg, and M. Tjernström, 2003: The turbulence structure of the stable atmospheric boundary layer around a coastal headland: Aircraft observations and modelling results. *Bound.-Layer Meteor.,* **107,** 531–559, doi:10.1023/A:1022822306571.

Brown, A., R. Beare, J. Edwards, A. Lock, S. Keogh, S. Milton, and D. Walters, 2008: Upgrades to the boundary layer scheme in the Met Office Numerical Weather Prediction model. *Bound.-Layer Meteor.,* **128,** 117–132, doi:10.1007/s10546-008-9275-0.

Canut, G., M. Lothon, F. Saïd, and F. Lohou, 2010: Observation of entrainment at the interface between monsoon flow and the Saharan air layer. *Quart. J. Roy. Meteor. Soc.,* **136,** 34–46, doi:10.1002/qj.471.

Conzemius, R. J., and E. Fedorovich, 2006: Dynamics of sheared convective boundary layer entrainment. Part I: Methodological background and large-eddy simulations. *J. Atmos. Sci.,* **63,** 1151–1178, doi:10.1175/JAS3691.1.

Couvreux, F., F. Guichard, A. Gounou, D. Bouniol, P. Peyrillé, and M. Köhler, 2014: Modelling of the thermodynamical diurnal cycle in the lower atmosphere: A joint evaluation of four contrasted regimes in the tropics over land. *Bound.-Layer Meteor.,* **150,** 185–214, doi:10.1007/s10546-013-9862-6.

Cuesta, J., and Coauthors, 2008: Multiplatform observations of the seasonal evolution of the Saharan atmospheric boundary layer in Tamanrasset, Algeria, in the framework of the African Monsoon Multidisciplinary Analysis field campaign conducted in 2006. *J. Geophys. Res.,* **113,** D00C07, doi:10.1029/2007JD009417.

——, J. H. Marsham, D. J. Parker, and C. Flamant, 2009: Dynamical mechanisms controlling the vertical redistribution of dust and the thermodynamic structure of the west Saharan atmospheric boundary layer during summer. *Atmos. Sci. Lett.,* **10,** 34–42, doi:10.1002/asl.207.

Deardorff, J. W., G. E. Willis, and B. H. Stockton, 1980: Laboratory studies of the entrainment zone of a convectively mixed layer. *J. Fluid Mech.,* **100,** 41–64, doi:10.1017/S0022112080001000.

Fiedler, S., K. Schepanski, B. Heinold, P. Knippertz, and I. Tegen, 2013: Climatology of nocturnal low-level jets over North Africa and implications for simulating mineral dust emission. *J. Geophys. Res. Atmos.,* **118,** 6100–6121, doi:10.1002/jgrd.50394.

Flamant, C., J. P. Chaboureau, D. J. Parker, C. A. Taylor, J. P. Cammas, O. Bock, F. Timouk, and J. Pelon, 2007: Airborne observations of the impact of a convective system on the planetary boundary layer thermodynamics and aerosol distribution in the inter-tropical discontinuity region of the West African monsoon. *Quart. J. Roy. Meteor. Soc.,* **133,** 1175–1189, doi:10.1002/qj.97.

Fochesatto, G. J., P. Drobinski, C. Flamant, D. Guedalia, C. Sarrat, P. H. Flamant, and J. Pelon, 2001: Evidence of dynamical coupling between the residual layer and the developing convective boundary layer. *Bound.-Layer Meteor.,* **99,** 451–464, doi:10.1023/A:1018935129006.

Galperin, B., S. Sukoriansky, and P. S. Anderson, 2007: On the critical Richardson number in stably stratified turbulence. *Atmos. Sci. Lett.,* **8,** 65–69, doi:10.1002/asl.153.

Gamo, M., 1996: Thickness of the dry convection and large-scale subsidence above deserts. *Bound.-Layer Meteor.,* **79,** 265–278, doi:10.1007/BF00119441.

Garcia-Carreras, L., J. H. Marsham, D. J. Bain, S. Milton, A. Saci, M. Salah-Ferroudj, B. Ouchene, and R. Washington, 2013: The impact of convective cold pool outflows on model biases in the Sahara. *Geophys. Res. Lett.,* **40,** 1647–1652, doi:10.1002/grl.50239.

Gray, M. E. B., J. Petch, S. H. Derbyshire, A. R. Brown, A. P. Lock, H. A. Swann, and P. R. A. Brown, 2001: Version 2.3 of the Met Office large eddy model. Part II: Scientific documentation. APR Turbulence and Diffusion Rep. 276, Met Office, 52. [Available online at http://appconv.metoffice.com/LEM/docs.html.]

Haywood, J., and O. Boucher, 2000: Estimates of the direct and indirect radiative forcing due to tropospheric aerosols: A review. *Rev. Geophys.,* **38,** 513–543, doi:10.1029/1999RG000078.

Huang, Q., J. H. Marsham, D. J. Parker, W. Tian, and C. M. Grams, 2010: Simulations of the effects of surface heat flux anomalies on stratification, convective growth, and vertical transport within the Saharan boundary layer. *J. Geophys. Res.,* **115,** D05201, doi:10.1029/2009JD012689.

Jickells, T. D., and Coauthors, 2005: Global iron connections between desert dust, ocean biogeochemistry, and climate. *Science,* **308,** 67–71, doi:10.1126/science.1105959.

Kaufman, Y. J., I. Koren, L. A. Remer, D. Rosenfeld, and Y. Rudich, 2005: The effect of smoke, dust, and pollution aerosol on shallow cloud development over the Atlantic Ocean. *Proc. Natl. Acad. Sci. USA,* **102,** 11 207–11 212, doi:10.1073/pnas.0505191102.

Lavaysse, C., C. Flamant, S. Janicot, D. J. Parker, J. P. Lafore, B. Sultan, and J. Pelon, 2009: Seasonal evolution of the West African heat low: A climatological perspective. *Climate Dyn.,* **33,** 313–330, doi:10.1007/s00382-009-0553-4.

Lock, A. P., A. R. Brown, M. R. Bush, G. M. Martin, and R. N. B. Smith, 2000: A new boundary layer mixing scheme. Part I: Scheme description and single-column model tests. *Mon. Wea. Rev.,* **128,** 3187–3199, doi:10.1175/1520-0493(2000)128<3187: ANBLMS>2.0.CO;2.

Marsham, J. H., D. J. Parker, C. M. Grams, B. T. Johnson, W. M. F. Grey, and A. N. Ross, 2008: Observations of mesoscale and boundary-layer scale circulations affecting dust transport and uplift over the Sahara. *Atmos. Chem. Phys.,* **8,** 6979–6993, doi:10.5194/acp-8-6979-2008.

——, P. Knippertz, N. Dixon, D. J. Parker, and G. M. S. Lister, 2011: The importance of the representation of deep convection for modeled dust-generating winds over West Africa during summer. *Geophys. Res. Lett.,* **38,** L16803, doi:10.1029/2011GL048368.

——, N. Dixon, L. Garcia-Carreras, G. M. S. Lister, D. J. Parker, P. Knippertz, and C. Birch, 2013a: The role of moist convection in the West African monsoon system: Insights from continental-scale convection-permitting simulations. *Geophys. Res. Lett.,* **40,** 1843–1849, doi:10.1002/grl.50347.

——, M. Hobby, C. J. T. Allen, J. R. Banks, M. Bart, B. J. Brooks, and R. Washington, 2013b: Meteorology and dust in the central Sahara: Observations from Fennec supersite-1 during the June 2011 intensive observation period. *J. Geophys. Res. Atmos.,* **118,** 4069–4089, doi:10.1002/jgrd.50211.

Matthews, A. J., and R. A. Madden, 2000: Observed propagation and structure of the 33-h atmospheric Kelvin wave. *J. Atmos. Sci.,* **57,** 3488–3497, doi:10.1175/1520-0469(2000)057<3488: OPASOT>2.0.CO;2.

Messager, C., D. Parker, O. Reitebuch, A. Agustí-Panareda, C. M. Taylor, and J. Cuesta, 2010: Structure and dynamics of the Saharan atmospheric boundary layer during the West African monsoon onset: Observations and analyses from the research flights of 14 and 17 July 2006. *Quart. J. Roy. Meteor. Soc.,* **136,** 107–124, doi:10.1002/qj.469.

Moeng, C.-H., and P. P. Sullivan, 1994: A comparison of shear- and buoyancy-driven planetary boundary layer flows. *J. Atmos. Sci.,* **51,** 999–1022, doi:10.1175/1520-0469(1994)051<0999: ACOSAB>2.0.CO;2.

Parker, D. J., and Coauthors, 2005: The diurnal cycle of the West African monsoon circulation. *Quart. J. Roy. Meteor. Soc.,* **131,** 2839–2860, doi:10.1256/qj.04.52.

Pino, D., J. Vila-Guerau de Arellano, and P. G. Duynkerke, 2003: The contribution of shear to the evolution of a convective boundary layer. *J. Atmos. Sci.,* **60,** 1913–1926, doi:10.1175/1520-0469(2003)060<1913:TCOSTT>2.0.CO;2.

Prospero, J. M., P. Ginoux, O. Torres, S. E. Nicholson, and T. E. Gill, 2002: Environmental characterization of global sources of atmospheric soil dust identified with the Nimbus 7 Total Ozone Mapping Spectrometer (TOMS) absorbing aerosol product. *Rev. Geophys.,* **40,** 1002, doi:10.1029/2000RG000095.

Roehrig, R., D. Bouniol, F. Guichard, F. Hourdin, and J. L. Redelsperger, 2013: The present and future of the West African monsoon: A process-oriented assessment of CMIP5 simulations along the AMMA transect. *J. Climate,* **26,** 6471–6505, doi:10.1175/JCLI-D-12-00505.1.

Ryder, C. L., and Coauthors, 2013: Optical properties of Saharan dust aerosol and contribution from the coarse mode as measured during the Fennec 2011 aircraft campaign. *Atmos. Chem. Phys.,* **13,** 303–325, doi:10.5194/acp-13-303-2013.

Stein, T. H. M., D. J. Parker, J. Delanoë, N. S. Dixon, R. J. Hogan, P. Knippertz, R. I. Maidment, and J. H. Marsham, 2011: The vertical cloud structure of the West African monsoon: A 4 year climatology using CloudSat and CALIPSO. *J. Geophys. Res.,* **116,** D22205, doi:10.1029/2011JD016029.

Stull, R., 1988: *An Introduction to Boundary Layer Meteorology.* Kluwer Academic, 666 pp.

Sullivan, P. P., C.-H. Moeng, B. Stevens, D. H. Lenschow, and S. H. Mayor, 1998: Structure of the entrainment zone capping the convective atmospheric boundary layer. *J. Atmos. Sci.,* **55,** 3042–3064, doi:10.1175/1520-0469(1998)055<3042: SOTEZC>2.0.CO;2.

Todd, M. C., and Coauthors, 2013: Meteorological and dust aerosol conditions over the western Saharan region observed at Fennec Supersite-2 during the intensive observation period in June 2011. *J. Geophys. Res. Atmos.,* **118,** 8426–8447, doi:10.1002/jgrd.50470.

Walters, D. N., and Coauthors, 2014: The Met Office Unified Model Global Atmosphere 4.0 and JULES Global Land 4.0 configurations. *Geosci. Model Dev.,* **7,** 361–386, doi:10.5194/gmd-7-361-2014.

Washington, R., M. Todd, N. J. Middleton, and A. S. Goudie, 2003: Dust-storm source areas determined by the total ozone monitoring spectrometer and surface observations. *Ann. Assoc. Amer. Geogr.,* **93,** 297–313, doi:10.1111/1467-8306.9302003.

——, and Coauthors, 2012: Fennec—The Saharan climate system. *CLIVAR Exchanges,* No. 60, International CLIVAR Project Office, Southampton, United Kingdom, 31–33. [Available online at http://www.clivar.org/sites/default/files/documents/Exchanges60.pdf.]

Weckwerth, T. M., J. W. Wilson, and R. M. Wakimoto, 1996: Thermodynamic variability within the convective boundary layer due to horizontal convective rolls. *Mon. Wea. Rev.,* **124,** 769–784, doi:10.1175/1520-0493(1996)124<0769:TVWTCB>2.0.CO;2.